ABSTRACT

Measuring Ice Accretion with a Microwave Radiometer

Tanner J. Trapp, M.S.E.C.E.

Mentor: B. Randall Jean, Ph.D.

Ice accretion inside jet engines is a major threat to modern aviation. Ice crystals in the atmosphere can be ingested by turbofan jet engines and build up inside reducing airflow through the engine. A reliable method to detect ice inside the engine before power loss occurs is needed. A passive microwave sensor has been developed to address this problem. The ice accretion sensor is a microwave radiometer which receives the natural thermal emissions of an environment. Ice emits high levels of energy compared to other materials at microwave frequencies making it highly detectable. The harsh measurement environment inside a jet engine has been addressed in the sensor design. Experimental results demonstrate the microwave radiometer's capability to detect ice accretion in an engine-like environment.

Measuring Ice Accretion with a Microwave Radiometer

by

Tanner Trapp, B.S.E.C.E

A Thesis

Approved by the Department of Electrical and Computer Engineering

_____

Kwang Y. Lee, Ph.D., Chairperson

Submitted to the Graduate Faculty of
Baylor University in Partial Fulfillment of the
Requirements for the Degree
of

Master of Science in Electrical and Computer Engineering

Approved by the Thesis Committee

_____

B. Randall Jean, Ph.D., Chairperson

_____

Yang Li, Ph.D.

_____

Stephen McClain, Ph.D.

Accepted by the Graduate School

May 2017

_____

J. Larry Lyon, Ph.D., Dean

Page bearing signatures is kept on file in the Graduate School.

TABLE OF CONTENTS

LIST OF FIGURES

LIST OF TABLES

ACKNOWLEDGMENTS

I would like to thank Dr. Jean, Dr. McClain, and Dr. Herrera for their guidance and direction. Thank you also to Chris Faulkner, George Toby, and Tim Shannon for their assistance. I would like to thank Mr. Ashley Orr. Lastly, I would like to thank DLT-2, LLC for their financial sponsorship of this work.

DEDICATION

To my wife, Sara

CHAPTER ONE

Introduction

Motivation

At altitudes above 22,000 ft, supercooled liquid water is extremely rare. Any moisture in the atmosphere is typically frozen into ice crystals, some as small as a few microns in diameter. Convective clouds, like those in a thunderstorm core, create air updrafts which carry moisture high into the atmosphere. Through the process of water rising past the point at which it can no longer exist in liquid form, areas with a high concentration of ice crystals form. Aircraft that fly through these high concentrations of ice crystals can experience ice accretion on the airframe. Though airframe icing can pose a problem to an aircraft, there are mechanisms by which the ice can be melted or shed while at altitude.

An even greater threat to aircraft, which has only been recognized in the past twenty years, is ice accretion inside a jet engine. Previously, engine ice accretion was thought to be impossible because ice would be shed by the high rotation speeds. Now, ice particle icing is recognized in the aviation industry as a real and dangerous problem. Ice crystals can be ingested by a turbofan jet engine where they can accrete either on stator vanes inside the low pressure compressor, or in engine ducts with a steep turning angle. Fig. 1 shows a schematic of a turbofan jet engine, and notes the locations where ice accretion can occur.

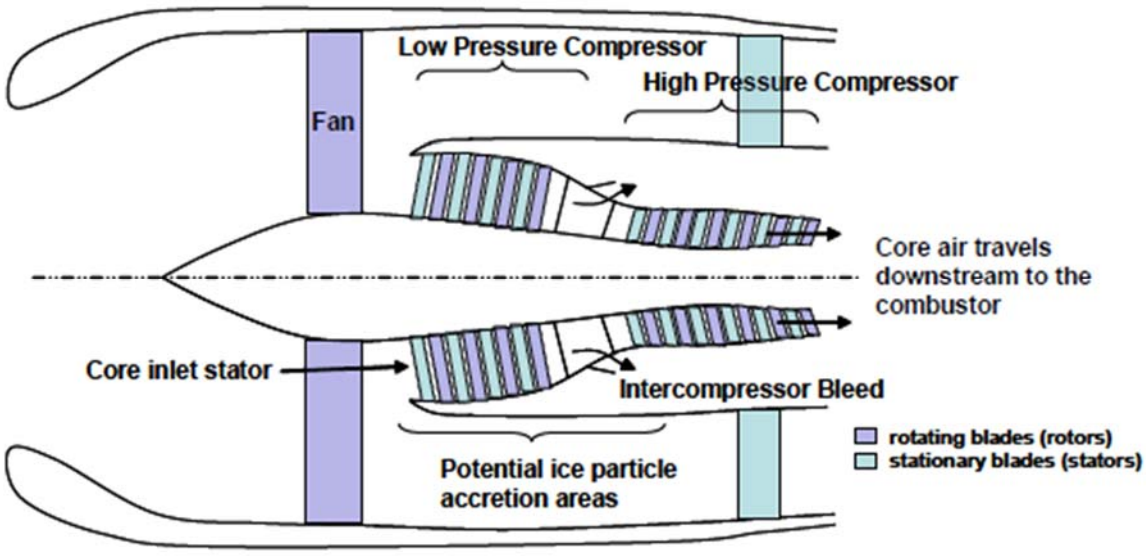

Fig. 1. Turbofan jet engine schematic *[1]*.

Ice accretion on stator vanes can occur when ice crystals melt as they pass through the rotors, but then refreeze on the stationary vanes that redirect engine airflow. Ice can accrete on engine ducts with a high turning angle because the ice crystals want to continue in a straight line through the engine [2]. Those crystals impact the cold duct surface, and can begin to accumulate there. If enough ice accretes, the engine will experience a *rollback*, or an uncommanded loss in engine thrust. Since the 1990's, there have been over 50 icing events in jet engine aircraft that have been attributed to ice accretion inside the engine [1]. There are several ways to shed ice inside the engine once it has accreted. First, the aircraft can descend to a lower altitude to reach warmer air. Second, hot air can be redirected from downstream in the engine to the low pressure compressor. Both of these maneuvers are costly in aircraft performance, and the shedding of ice inside an engine can cause damage to downstream components.

Ice accretion inside a jet engine is particularly dangerous because it can occur without other external factors present, like the presence of supercooled liquid water. In

addition, ice accretion inside an engine can only be detected by a change in engine performance. To reach that point, however, a significant amount of ice had to have already accreted. Current sensing methods, like a Rosemount ice detector, are only designed to measure airframe ice accretion [3]. The ice particles alone are difficult to detect in the atmosphere with radars as well because of insufficient scattering.

A sensor that can reliably detect engine ice accretion would need to be implemented inside the engine. Adapting a sensor so that it can survive the temperatures and pressures inside the compressor stage of a jet engine is non-trivial. The work presented here describes the design and testing of an ice accretion sensor that has been ruggedized to survive inside a jet engine.

CHAPTER TWO

Technical Background

To explain the sensor that has been developed, the underlying concepts are presented first. The following sections are an overview of microwave radiometry and material properties that are pertinent to the work. Further information about the development of the ice accretion sensor can be found in Chapter Three and Chapter Four.

Microwave Radiometry

A microwave radiometer is a passive sensor that detects the natural thermal radiation of objects in the microwave frequency range. In essence, a microwave radiometer remotely measures power emitted by objects in its antenna's field of view. Everything in the universe that has an absolute temperature above 0° K is emitting some level of radiation. If an object is in thermal equilibrium, this also means that the object is absorbing an equivalent amount of radiation as it is emitting.

Often times when dealing with radiometric systems, the power detected is measured in terms of a brightness temperature [4, p. 7]. This quantity is the physical temperature of a *blackbody* that would radiate the same amount of power. A blackbody is an object that absorbs all radiation incident upon it, which also means it emits the same amount. The power of blackbody radiation is given by

$$P = kTB. \tag{1}$$

For a given temperature a blackbody will emit more power than any other object. Understanding blackbody radiation is important to the design of radiometric systems. The intensity of blackbody radiation is given by Planck's Law.

$$B_f(T) = \frac{2hf^3}{c^2 e^{\left(\frac{hf}{k_B T}\right)} - 1} \tag{2}$$

$B_f(T)$, also known as the radiance, is a function of both temperature and frequency, and is given in units of W/m^2·sr·Hz. In (4), h is the Planck constant (6.626 x 10^{-23} m^2·kg/s), f is the frequency in Hertz, c is the speed of light in vacuum (2.998 x 10^8 m/s), k_B is the Boltzmann constant (1.381 x 10^{-23} m^2·kg/s^2·K), and T is the physical temperature in Kelvin. Several radiation curves for different temperatures are shown in Fig. 2. The radiation intensity, referred to as brightness in the Fig. 2, is given in terms of frequency (left vertical axis) as well as wavelength (right vertical axis).

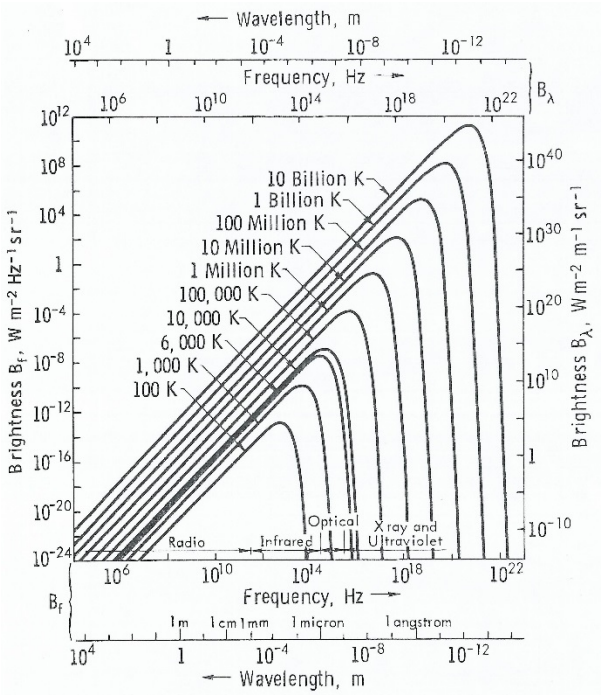

Fig. 2. Planck's Law radiation curves as a function of frequency and temperature *[5, p. 456]*.

Brightness temperature is directly proportional to the physical temperature. For each temperature there also exists an absolute maximum radiance at a particular frequency. There is a region for each temperature, at frequencies lower than the maximum brightness frequency, where the brightness appears to be linear. For these low frequencies, or large wavelengths, Planck's Law can be rewritten in the following form:

$$B_f(T) = \frac{2k_B f^2 T}{c^2}. \tag{3}$$

Equation (3), known as the Rayleigh-Jeans Law, describes the intensity of blackbody radiation, but is only valid for low frequencies. The condition for applying the Rayleigh-Jeans Law approximation to Planck's Law is $hf << k_B T$, which is satisfied at microwave frequencies. Having a basic understanding of thermal radiation, the equations associated with a radiometer can now be discussed.

A radiometer measures the brightness temperature from its antenna in a certain bandwidth. A radiometer with bandwidth B measures an output power of

$$P = kBGT_A. \tag{4}$$

G is the gain of the radiometer, k is the Boltzmann constant as seen previously in (3), and T_A is the brightness temperature seen by the antenna. The brightness temperature is related to physical temperature by a parameter called *emissivity*.

$$e = \frac{T_b}{T} \tag{5}$$

Emissivity can also be thought of as the ratio of an object's radiation to the radiation of a blackbody at the same temperature. A non-blackbody object can have an emissivity between $0 \leq e \leq 1$, with a blackbody having $e = 1$. Using (5), an equivalent expression for the output power of a radiometer is

$$P = ekBGT. \tag{6}$$

Now the power received by a radiometer is expressed in terms of physical temperature and emissivity. Though the output power is measured in Watts, a typical radiometer deals with output power on the order of 1 x 10^{-12} W, or -90 dBm (decibels with respect to one milliwatt). The components of a radiometer also emit thermal radiation which adds noise to the system. An additional noise term, T_N, is added to account for this reality so (4) becomes

$$P = kBG(T_A + T_N). \tag{7}$$

The sensitivity of a microwave radiometer is an important design consideration. A radiometer's sensitivity describes the smallest change in physical temperature that it can detect, and is given by the following equation. The mathematical development of the radiometer sensitivity equation is lengthy and has been omitted for brevity.

$$\Delta T = \frac{T_A + T_N}{\sqrt{B \cdot \tau}} \tag{8}$$

The integration time, τ, describes how long the receiver is collecting radiation from the antenna. Both a longer integration time and larger bandwidth will increase the sensitivity. The desired sensitivity in a microwave radiometer is heavily dependent upon the application, though typically is not more than a few Kelvin.

Dicke Radiometer

One particular kind of radiometer was conceived by R. H. Dicke in 1946 which came to be known as the Dicke radiometer [6]. Whereas other radiometers try to directly measure the radiated power from an object, the Dicke radiometer compares the radiated power from an object with a known reference load. This reference load is maintained at a

stable temperature so that its thermal radiation is constant. The radiometer switches between receiving power from the antenna and reference at a frequency, F_s, on the order of 1 kHz. One downside of the Dicke radiometer is the halving of the integration time. This degrades the radiometer's sensitivity which can be seen in (9).

$$\Delta T = \frac{T_A + T_N}{\sqrt{B \cdot \tau/2}} \tag{9}$$

The benefit of comparing to a reference load, however is greater immunity to instability in the system. If the switching frequency is fast enough, parameters like gain and noise temperature can be treated as constants. Fig. 3 shows a typical block diagram of a Dicke radiometer.

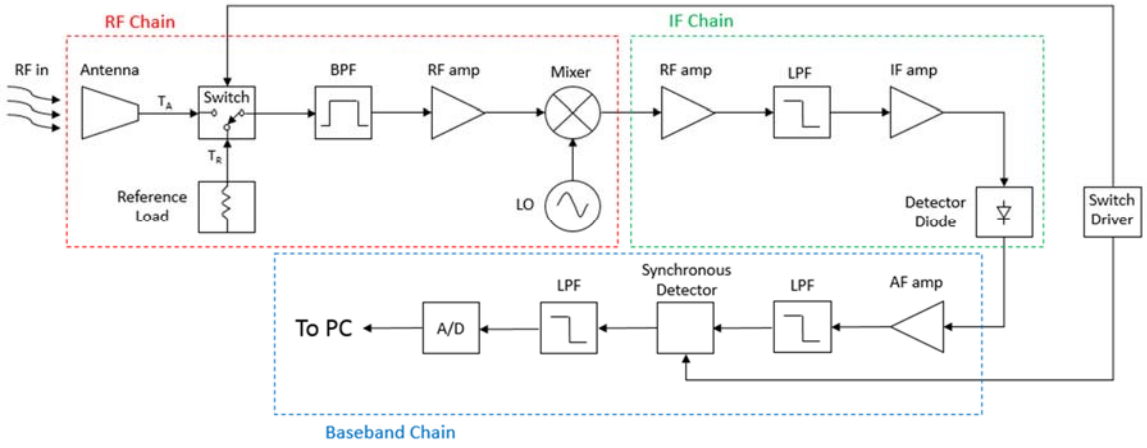

Fig. 3. Block diagram of Dicke radiometer. Designations for RF chain, IF chain, and Baseband chain are shown for clarity.

The local oscillator (LO) in the RF chain sets the center frequency of the radiometer. Whichever filter before the diode detector has the narrowest bandwidth sets the radiometer bandwidth, B. The RF switch and synchronous detector are both controlled by a switch driver. The driver sets the switching frequency, and determines if the radiometer is connected to the antenna or reference load. The detector diode converts

the signal to DC by keeping the envelope of the high frequency signal. The signal gets AC coupled before entering the synchronous detector to remove the DC offset. All that remains of the signal now are two voltage levels; one from the reference load, and the other from the antenna. Averaging and other post-processing may take place to get a consistent value for both voltages. Fig. 4 [4] shows the signal before and after the detector diode, as well as after AC coupling.

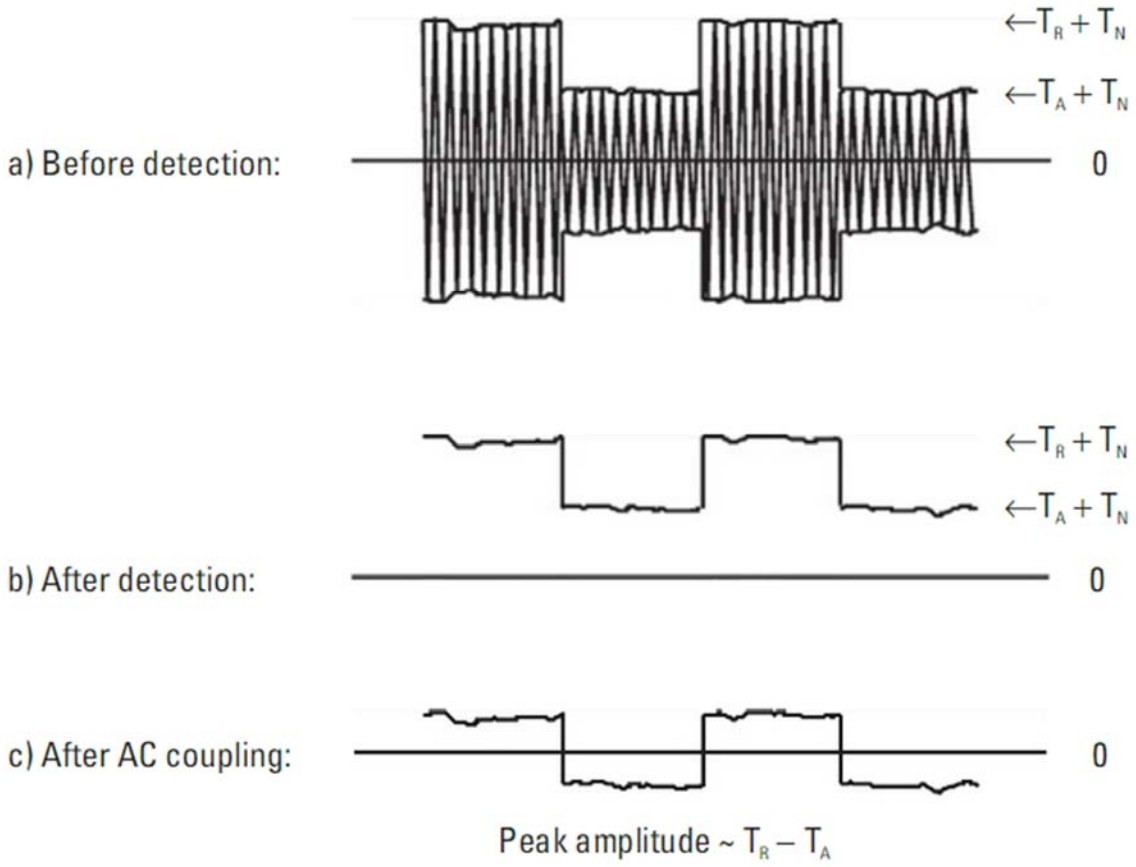

Fig. 4. Dicke radiometer signal (a) Before diode detector. (b) After diode detector. (c) After AC coupling.

The horizontal axes in Fig. 4 are time, and the vertical axes are voltages. The square wave that is created by the switch driver has a period of $2/F_s$. Ultimately, the computer will record the difference in voltages between the antenna and reference load.

The microwave radiometer will have been calibrated in a controlled environment. The computer can interpolate the voltage data to determine the approximate physical temperature of the environment. Other material properties, like emissivity or moisture content, can also be extrapolated using a microwave radiometer.

Material Properties

Microwave sensing and measuring has just as much to do with material properties as it does with the sensor itself. In fact, a good sensor design cannot be achieved without a thorough understanding of material properties. At a fundamental level, there are two outcomes brought about by material properties, energy storage or energy dissipation. Most materials encountered in microwave sensor design can be categorized as either dielectrics or conductors. A dielectric is a material whose dominant charges are bound, meaning they are held in place by atomic and molecular forces [7]. This characteristic of a dielectric allows electromagnetic energy to propagate in it without energy dissipation. Conversely, a conductor has free charges that prevent it from being polarized like a dielectric. As a result, conductors dissipate electromagnetic energy very quickly in the microwave frequency range. Common conductors used in microwave designs are aluminum, copper, and brass. The microwave frequency range is sometimes defined to be between 300 MHz (3×10^8 Hz) and 300 GHz (3×10^{11} Hz), which corresponds to wavelengths between 1 m and 1 mm [8, p. 1].

There are two different mechanisms by which a material can store or dissipate electromagnetic energy. The first mechanism is electric energy storage and dissipation which is characterized by *permittivity*, ε. Permittivity also relates the electric flux density, D, to the electric field intensity, E, in the following constitutive relationship:

$$D = \varepsilon \cdot E. \tag{10}$$

Permittivity can be mathematically expressed in several different ways depending upon the application. Two of these expressions are shown in (11) and (12).

$$\varepsilon = \varepsilon_r \varepsilon_0 \tag{11}$$

$$\varepsilon = \varepsilon' - j\varepsilon'' \tag{12}$$

Equation (11) relates the permittivity of a material to the permittivity of free space (ε_0 = 8.854 x 10^{-12} F/m) by the relative permittivity, ε_r, also known as the dielectric constant. The expression in (12) separates the permittivity into the energy storage component, ε', and the energy dissipation (lossy) component, ε''. An ideal dielectric will have some $\varepsilon_r' > 1$, and $\varepsilon_r'' = 0$. Real dielectrics, however, will have some loss associated with their permittivity. Losses in dielectrics are discussed in terms of their *loss tangent,* seen in (13).

$$\tan\delta = \frac{\omega\varepsilon'' + \sigma}{\omega\varepsilon'} \tag{13}$$

The loss tangent is a ratio of the real to imaginary part of the permittivity [8, p. 10]. It also depends upon the *conductivity*, σ, which describes the free electron movement in a material. The higher the loss tangent of a material, the more loss of energy there will be in the material. Conductors have high losses at microwave frequencies because of their high conductivity.

The second mechanism for energy storage and dissipation is magnetic. In the same way that permittivity describes a material's electric properties, *permeability* (denoted by μ) describes a material's magnetic energy storage and dissipation. Equation (14) shows the equivalent constitutive relationship for the magnetic flux density, B, and magnetic field intensity, H.

$$B = \mu \cdot H \tag{14}$$

Similar to permittivity, there are multiple expressions for the permeability, some of which can be seen below.

$$\mu = \mu_r \mu_0 \tag{15}$$

$$\mu = \mu' - j\mu'' \tag{16}$$

The same relationships apply to permeability as they did to permittivity, where μ_r is the relative permeability, and μ_0 is the permeability of free space (4π x 10^{-7} H/m). Additionally, μ' is the magnetic energy storage component, and μ'' is the magnetic energy dissipation component. Most dielectrics are non-magnetic materials ($\mu_r = 1$) so dealing with permeability is not as common in microwave sensor design.

Properties of Water

One of the difficulties in making an ice accretion measurement inside a jet engine is determining the difference between water and ice. Understanding the unique material properties of water is the first step in overcoming this difficulty. Perhaps the single biggest contributor to water's unique properties is its molecular polarity. The two hydrogen atoms form a positive pole, and the oxygen atom forms a negative pole. As a result, water has a very high relative permittivity compared to other naturally occurring substances. Water's high dielectric constant also means it has a low emissivity, around 0.4. A plot of water's complex permittivity over frequency can be seen in Fig. 5. It should be noted that this data represents water at 25°C. Permittivity, as well as other material properties, is dependent upon temperature. In general, as temperature decreases, so does a material's permittivity.

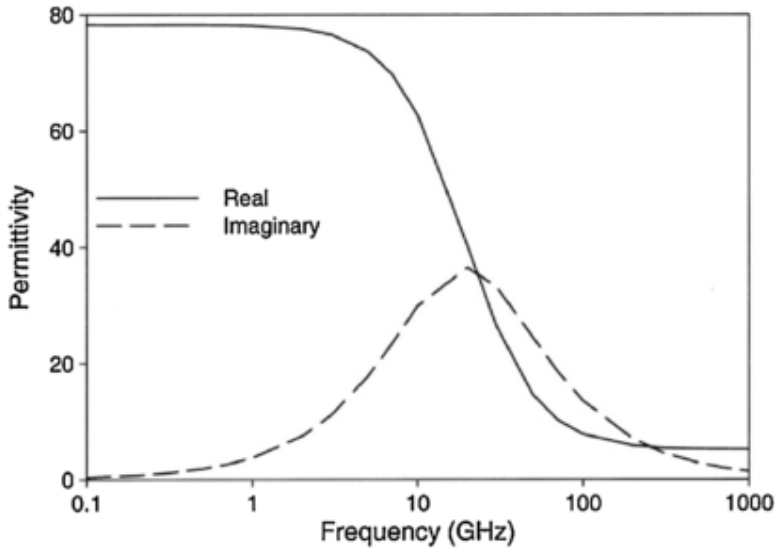

Fig. 5. Complex permittivity of water versus frequency at 25°C *[9]*.

In the low GHz range, water has a real part of the relative permittivity of about 75. There is a drop off that occurs in the mid-GHz range, with an inflexion point at approximately 22 GHz. This inflexion point, also called the *relaxation frequency*, is at the same frequency as the maximum of the imaginary part of the permittivity [10]. The above model was developed by Peter Debye in 1929 [11], and is given by the following equation:

$$\varepsilon(\omega) = \varepsilon_\infty + \frac{\varepsilon_s - \varepsilon_\infty}{1 + j\omega\tau}. \tag{17}$$

The Debye relaxation model is commonly used for describing dielectric spectra. In (17), the permittivity at a particular frequency, ε, is defined by its static permittivity, ε_s, and its permittivity at infinite (or very large) frequency, ε_∞. The other important parameter is the relaxation time constant, τ, which is the inverse of the relaxation frequency. Properly understanding the unique dielectric spectrum of water informs a microwave sensor design that will interact with water. In the context of this project, the dielectric spectra of water near 0°C was of particular interest. The relaxation frequency of

water near 0°C is cited in the literature as being about 10-12 GHz [12]. Having maximal dielectric losses would also make water easy to distinguish with a microwave radiometer. Therefore, 10 GHz was an early candidate for the radiometer's center frequency.

Properties of Ice

Though molecularly ice and water are identical, their material properties are quite different. The crystalline structure of ice affects how energy can be stored and dissipated. Fig. 6 shows the real part of the relative permittivity of ice versus frequency for multiple temperatures.

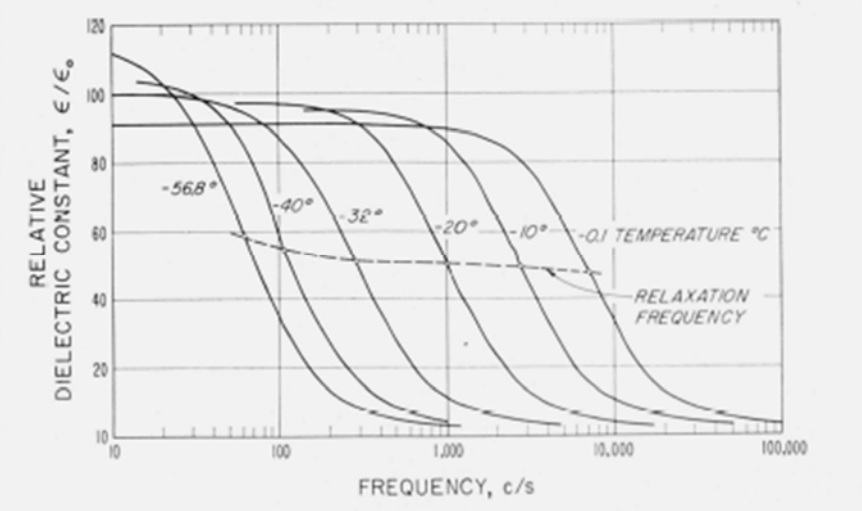

Fig. 6. Real part of the relative permittivity of ice versus frequency. Permittivity data is shown for multiple temperatures *[13]*.

Compared to water, the relaxation frequency of ice is several orders of magnitude lower. In the microwave frequency range ice has a relative permittivity of 3.17 [14]. The loss tangent of ice in the microwave frequency range is also very low because it has its maximum at the relaxation frequency. Ice has a much higher emissivity than water making it easy to detect with a microwave radiometer. Measurements by well-calibrated

radiometers have determined the emissivity of ice to be between 0.85-0.95 depending upon its age [15]. Ice's material properties are also polarization dependent because of its crystalline structure [16]. The effects of polarization have not been studied thoroughly in this work, but will be in the future.

CHAPTER THREE

Ice Accretion Sensor Design

A microwave radiometer has been developed to measure ice accretion inside a turbofan jet engine. There are several reasons why a microwave radiometer was chosen over other microwave sensing methods. First, a microwave radiometer is a passive sensor. Other sensors would need to transmit energy into the engine where it can be distorted by the Doppler shift caused by the spinning rotors. As ice builds up it is also emitting thermal radiation. A microwave radiometer can sense the change in thermal radiation caused by the presence of the ice. It does not matter if that energy is actually being emitted at a lower frequency then shifted up by the spinning blades. Second, the radiometer antenna can be ruggedized to survive inside a jet engine. The rest of the system can be located elsewhere, away from the engine. Multiple considerations have been made regarding the radiometer antenna, and will be discussed later in this chapter. Third, the radiometer antenna aperture can be small, less than 0.5 in^2. It was necessary to avoid cutting a large hole in the side of a jet engine for obvious reasons. The following section outlines the major components of the microwave radiometer, and its performance.

Microwave Radiometer Design

The initial design of the microwave radiometer system was developed by Ballew in 2006 [17]. Its operating frequency range was 4.5 – 6.5 GHz, and was intended for biomedical applications. For this project, however, a wide-band microwave radiometer was desired to study the radiation of water and ice at multiple frequencies. The design of

the microwave radiometer could be broken down into three major sections: the radio frequency (RF) chain, the intermediate frequency (IF) chain, and the baseband chain. The first component in the RF chain after the antenna was the Dicke switch. An Analog Devices HMC-C011 single-pole double-throw (SPDT) switch was chosen because of its high isolation (>35 dB up to 20 GHz) and low insertion loss (2 dB at 12 GHz). The switching frequency was set to 500 Hz to minimize gain fluctuations. One input to the Dicke switch was from the antenna, and the other input was a high power capacity 50 Ω termination which served as the reference load. The next component after the Dicke switch was the RF amplifier. Typically in a radiometer design, there is a bandpass filter before the RF amplifier that sets the radiometer bandwidth. The initial design, however, was focused on multi-band capability. An RF filter would be added once the center frequencies were determined. The RF amplifier was particularly important to the design because it had the greatest effect on the radiometer's sensitivity. A Mini-Circuits ZVA-213+ Super Ultra-Wideband Amplifier was chosen. It provided 26 dB of gain, and had a low noise figure of 3.0 dB. After the RF amplifier, the signal was then down-converted using a Mini-Circuits ZX05-24MH+ wideband frequency mixer. The mixer combined the signal from the RF amplifier, and the signal from the local oscillator (LO). An HP-8720ET Vector Network Analyzer (VNA) was used as the LO. The VNA provided a continuous wave output with a power of +10 dBm, and gave the ability to switch the radiometer's center frequency easily.

After down-conversion, the first component of the IF chain was the IF amplifier. An Amplical AMP001G2-30 broadband amplifier provided 30 dB of gain with a noise figure of 2.5 dB. Due to the high gain of the RF amplifier, however, the noise figure and

insertion losses of components after the RF amplifier were insignificant. The next component was a low-pass filter from Lorch Microwave with a cutoff frequency of 600 MHz. The low-pass filter sets the radiometer bandwidth to 1200 MHz because it was a dual-sideband radiometer. The last two components of the IF chain were two cascaded IF amplifiers from Mini-Circuits that each added 12 dB of gain.

The baseband chain began with a detector diode. Fig. 4 (b) in Chapter Two shows how the diode detector captures the envelope of the IF signal input to it, converting it to a DC signal. Other components in the baseband chain included an instrumentation amplifier, and additional low-pass filters to eliminate high frequency noise. The signal passed through a synchronous detector that was driven by the same switch driver as the RF switch. For in-lab testing, a stand-alone function generator served as the switch driver. The final signal output was displayed on a LeCroy HDO4508 oscilloscope, and transferred to a computer via USB. For a list of the major components used in the design, see Appendix B.

Performance Calculations

Calculations were done to evaluate the microwave radiometer design's performance. The first metric calculated was the radiometer's sensitivity. To calculate the sensitivity, first the front end noise figure had to be found. For a generic system, the noise figure is calculated by the following expression.

$$F_{total} = F_1 + \frac{F_2 - 1}{G_1} + \frac{F_3 - 1}{G_1 G_2} + \cdots \tag{18}$$

If the first gain element is sufficiently large, the subsequent noise figures have almost no impact on the system's noise figure. In this case, G_1 = 26 dB (398.1 on a linear

scale) from the RF amplifier. Bearing this in mind, calculating the noise figure of the system was simply a matter of adding the noise figures and insertion losses of components up to and including the RF amplifier. These values can be seen in Table 1.

Table 1. Noise figure calculation for microwave radiometer

Component	Noise Figure or Insertion Loss
Dicke Switch	2.0 dB
RF Amplifier	3.0 dB
Total	5.0 dB

Now, the system noise temperature could be calculated by the following expression in (19) [4, p. 29]. Equation (19) used the noise figure on a linear scale (5.0 dB converts to 3.16 linear).

$$T_N = 290(NF - 1) = 290(3.16 - 1) = 626.4 \tag{19}$$

The calculation in (18) assumed a noiseless antenna though this is not the case in a real measurement scenario. With a noise temperature of 626.4 K, the microwave radiometer's sensitivity at room temperature (T_A = 300 K) was given by

$$\Delta T = \frac{300 + 626.4}{\sqrt{600 \times 10^6 * 0.5}} = 0.0535\ K \tag{20}$$

The second metric calculated was a combination of the input power, system gain, and output signal level. A blackbody will radiate energy as calculated by

$$\mathrm{P} = \mathrm{kTB}. \tag{21}$$

For a blackbody at 300 K (room temperature) and a 1.2 GHz bandwidth, the power radiated by a blackbody is -83 dBm. Any real object will emit less power in accordance with its emissivity, but examining blackbody radiation was sufficient for understanding the radiometer's performance. The total radiometer gain (up to the detector

diode) of 82 dB nominally, and an estimated 17 dB of losses through the system resulted in a realized gain of 65 dB. Therefore the output signal level going into the detector diode was approximately -18 dBm. This power level was sufficient to operate the detector diode in the square-law region.

Measurement Environment Considerations

Water and ice have long been measured using radiometric systems [18] [19] [20]. The uniqueness of this measurement problem was the environment in which it must take place. Inside the compressor stage of a turbofan jet engine temperatures range from -40°C to 200°C, and pressures are significant. In addition to the temperature and pressure, the sensor size and location were important to consider. Any aperture cut into the wall of the engine must not only be small, but also must be filled in with a process seal. The sensor itself could not protrude into the compressor stage airflow, and could not extend too far on the other side into the bypass airflow. A typical microwave sensor cannot survive, much less take accurate data in such conditions. To make an ice accretion sensor viable for implementation inside a jet engine, there needed to be significant design modifications. The following sections explain the test set-up and ways in which the microwave radiometer has been adapted to handle this environment.

Stator Vane Assembly

The first obstacle to overcome in designing a sensor for the inside of a jet engine was matching the geometry. Microwave sensor designs depend heavily upon the size, shape, and material properties of where they will be implemented. The same held true for a microwave radiometer that was intended for measurements inside the compressor stage

of a jet engine. A mechanical stator vane assembly was fabricated to model the exit guide vanes of a turbofan jet engine where ice is known to accrete [21]. The exit guide vanes are the last row of stator vanes in the compressor stages of a jet engine. After this row of stator vanes, there is typically a duct with a high turning angle. Fig. 7 shows the fabricated stator vane assembly.

Fig. 7. Stator vane assembly modeled after exit guide vanes.

The stator vane assembly was made of aluminum, and consisted of five vanes and four passages. A detailed mechanical drawing of the stator vane assembly with dimensions can be found in Appendix A. Aluminum was used because it is a machinable metal and would not easily rust. Two of the passages had square grooves cut in the bottom sheet to test how they would change the emissions from ice and water. During manufacturing, however, square grooves were cut instead of the preferred V-shaped grooves. Measurement results were not significantly different for passages with grooves

or without grooves. Each passage had an aperture cut out of the top sheet, which can be better seen in Fig. 8. The circular holes around each aperture were threaded to secure the microwave radiometer antenna in place for testing.

Fig. 8. Top view of stator vane assembly. This view is shown to highlight the apertures above the passages. The threaded holes seen around the main apertures were used to connect to WR-90 flanges.

The apertures were cut to a size of 0.4 in wide by 0.9 in long to fit WR-90 waveguide components. WR-90 is a dimensional standard for rectangular waveguides that operate from 8.2 – 12.4 GHz. These dimensions were small enough for the jet engine, but still allowed for effective electromagnetic coupling out of the environment. Two of the apertures were rotated by 90° to test polarization effects. The stator vane assembly allowed for testing multiple antennas and ice accretion testing in a controlled environment that closely modeled actual engine geometries.

Process Seal Insert for Waveguide-to-Coax Adapter

The first antenna tested was a standard waveguide-to-coax adapter. It conveniently transitioned from coaxial cable to the WR-90 apertures in the stator vane assembly. In a real engine, however, the air cavity inside a waveguide-to-coax adapter would be unacceptable. If a waveguide-to-coax adapter were to be used, there would need to be a process seal insert to fill the adapter. The insert would need to not only

handle the temperatures and pressures inside the compressor stage of a jet engine, but also have favorable electromagnetic properties (i.e. low dielectric constant, low loss, etc.).

A suitable choice of material for the process seal insert was MACOR machinable glass ceramic. MACOR has a dielectric constant of 5.64 and a loss tangent of 0.0025, measured at 8.5 GHz. It also can survive the pressure inside the engine with a compressive strength of 345 MPa. MACOR's machinability was also important for manipulating its geometry. The first design of a process seal insert was a total fill of a waveguide-to-coax adapter. A 3D model of a total MACOR fill of a WR-90 waveguide-to-coax adapter can be seen in Fig. 9.

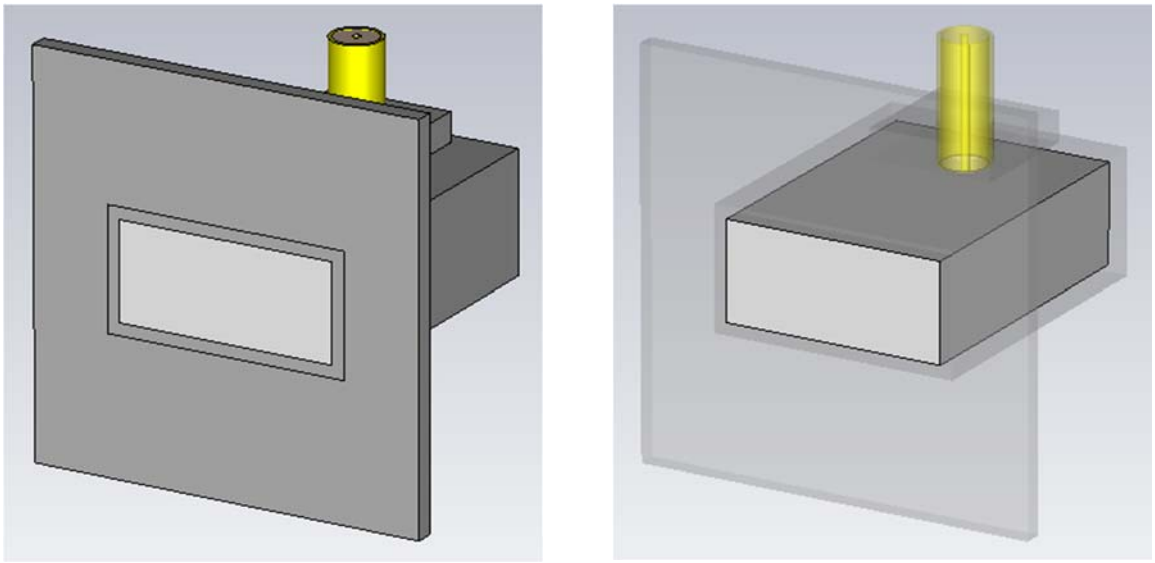

Fig. 9. WR-90 waveguide-to-coax adapter filled with MACOR. (a) Perspective view. (b) Perspective view with MACOR block highlighted.

The model was created in CST Microwave Studio (CST MWS), which is a 3D electromagnetic solver software [22]. A total MACOR fill was easy to implement, but overlooked important design parameters of the waveguide-to-coax adapter. The distance

from the coaxial probe to the back wall of a waveguide-to-coax adapter, or *back-short distance*, is a function of wavelength. In a dielectric with permittivity different than air, the wavelength will change by the square root of the relative permittivity. Also, the distance the coaxial probe extends into the adapter, or *probe length*, depends upon the wavelength. These two parameters would need to be re-tuned for the process seal insert to achieve good performance. For a primary test of the MACOR process seal insert, however, the waveguide-to-coax adapter was not modified.

Two waveguide-to-coax adapters were connected to test the effect of a total process seal insert. Measurements were taken using an Agilent PNA-L N5230C VNA. The measurement results of a total MACOR fill in both adapters were compared to the performance of unfilled waveguide-to-coax-adapters. A plot of S_{21} for both MACOR to MACOR and air to air can be seen in Fig. 10.

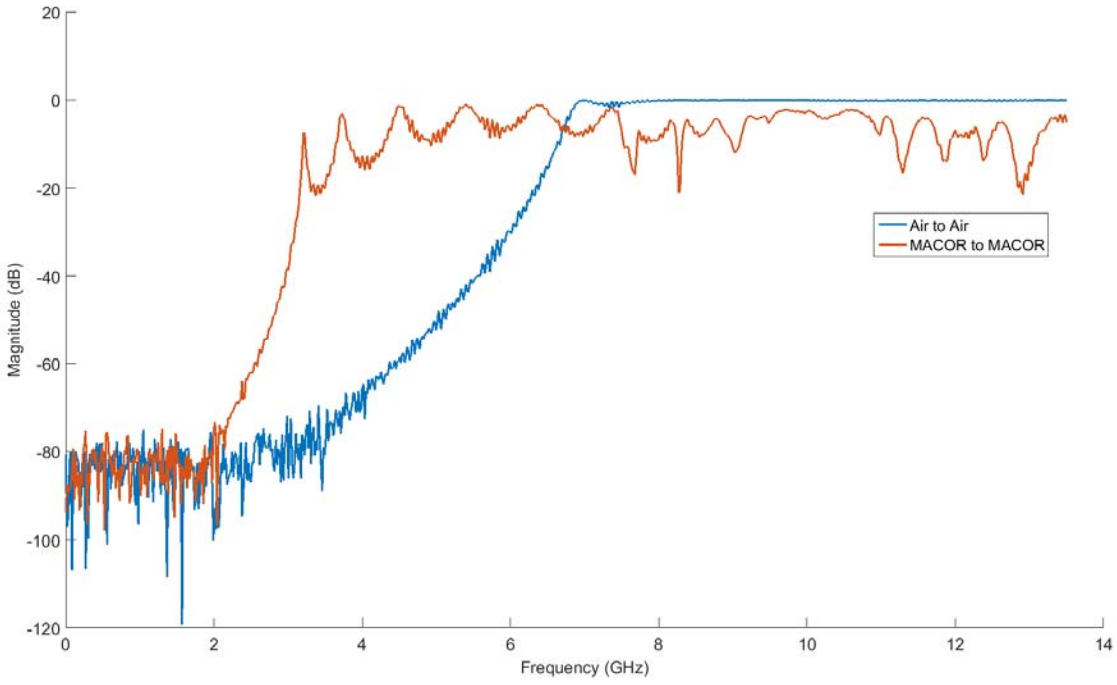

Fig. 10. S_{21} comparison of MACOR filled to un-filled waveguide-to-coax adapter.

The S_{21} of the MACOR to MACOR measurement had several interesting features. First, the fundamental mode cutoff frequency was lower than the air-filled waveguide-to-coax adapters. The cutoff frequency of a rectangular waveguide depends upon the relative permittivity of what's inside it, so this results was expected [7, p. 356]. Second, the MACOR to MACOR had significant passband ripple. Unlike the air to air measurement which has a steady S_{21}, the MACOR to MACOR measurement varied over frequency. As previously mentioned, there was no change to the back-short distance for this process seal insert. An incorrect back-short distance can degrade the performance of the waveguide-to-coax adapter because of impedance mismatch. Third, the dielectric loss in the MACOR attenuated the signal. At 10 GHz, where there was minimal ripple in the S_{21}, the signal level was still 2.8 dB lower than the air to air measurement. As a result, a process seal insert that completely fills the waveguide-to-coax adapter was not viable. This conclusion was further demonstrated by a radiometer experiment whose results are shown in Chapter Four.

The second design of a process seal insert for a waveguide-to-coax adapter modified the geometry of the insert. The goal of this design was to reduce the dielectric loss of the process seal insert by only partially filling the adapter. To minimize impact on performance, the process seal insert was also removed from around the coaxial probe. By doing so, the back-short distance and probe length did not need to be adjusted. The geometries created a smooth transition inside the waveguide-to-coax adapter from air to MACOR. An abrupt change, like the one created by a total MACOR fill, caused strong reflections at the interface. Several geometries were simulated, including a triangular geometry, an elliptical geometry, and an ogee geometry. CST MWS models of the three

process seal insert geometries can be seen in Fig. 11. The three geometries were simulated, and their S-parameter results are shown in Fig. 12, Fig. 13, and Fig. 14.

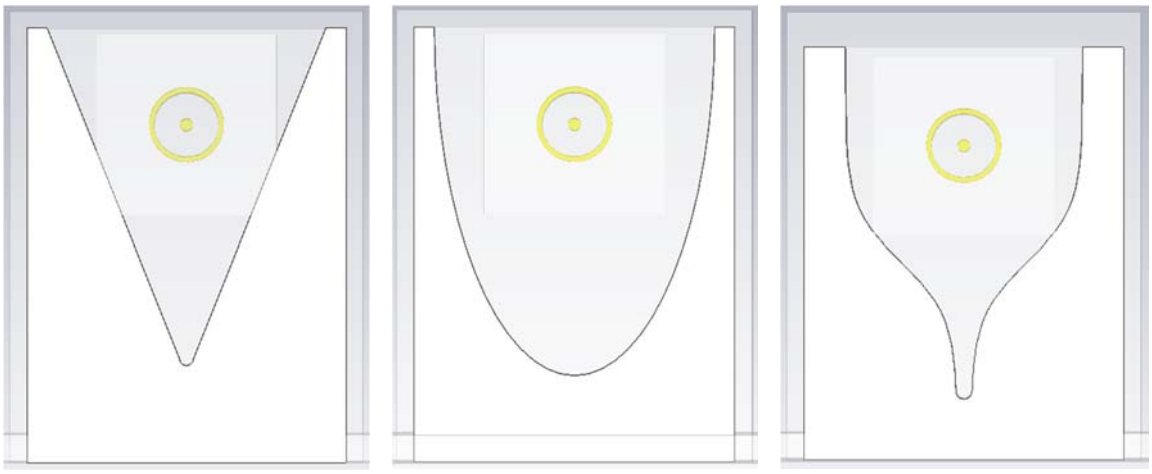

Fig. 11. Top view of modified process seal inserts for a waveguide-to-coax adapter. (a) Triangular geometry. (b) Elliptical geometry. (c) Ogee geometry.

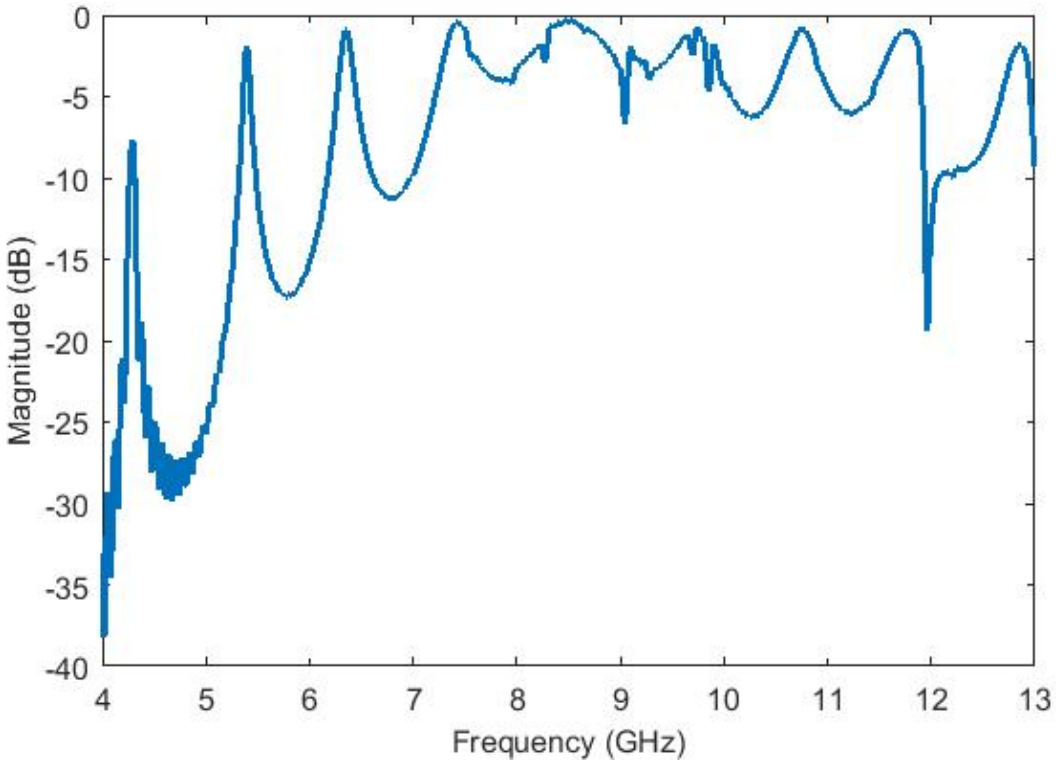

Fig. 12. S_{21} of triangular geometry process seal insert for waveguide-to-coax adapter.

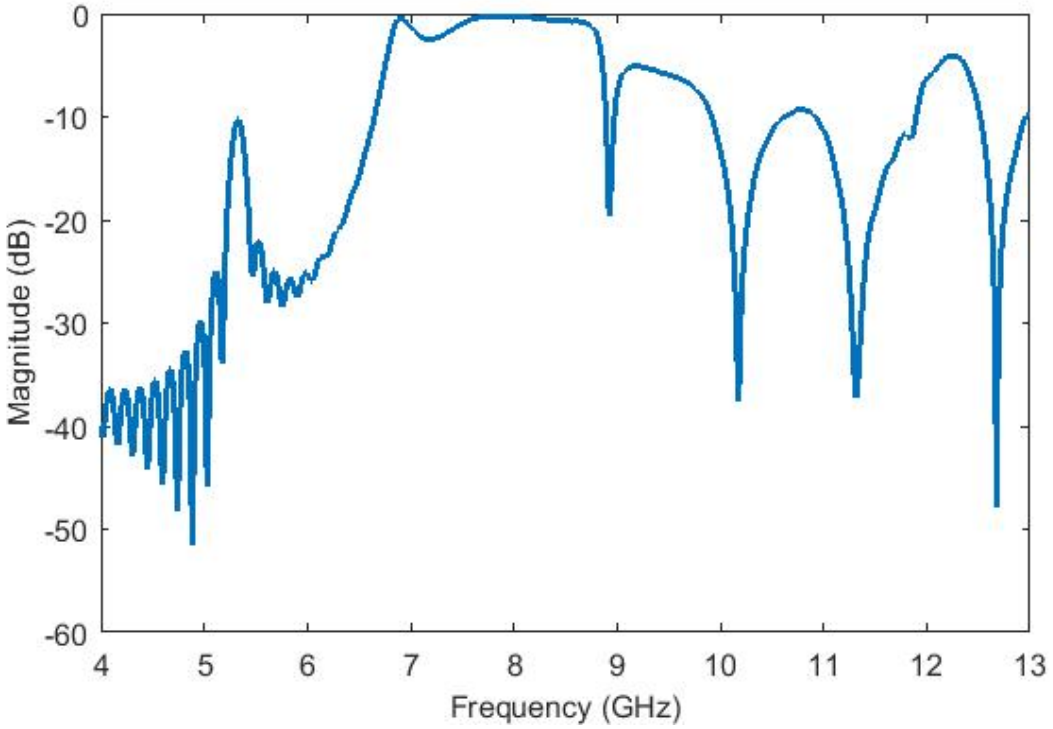

Fig. 13. S_{21} of elliptical geometry process seal insert for waveguide-to-coax adapter.

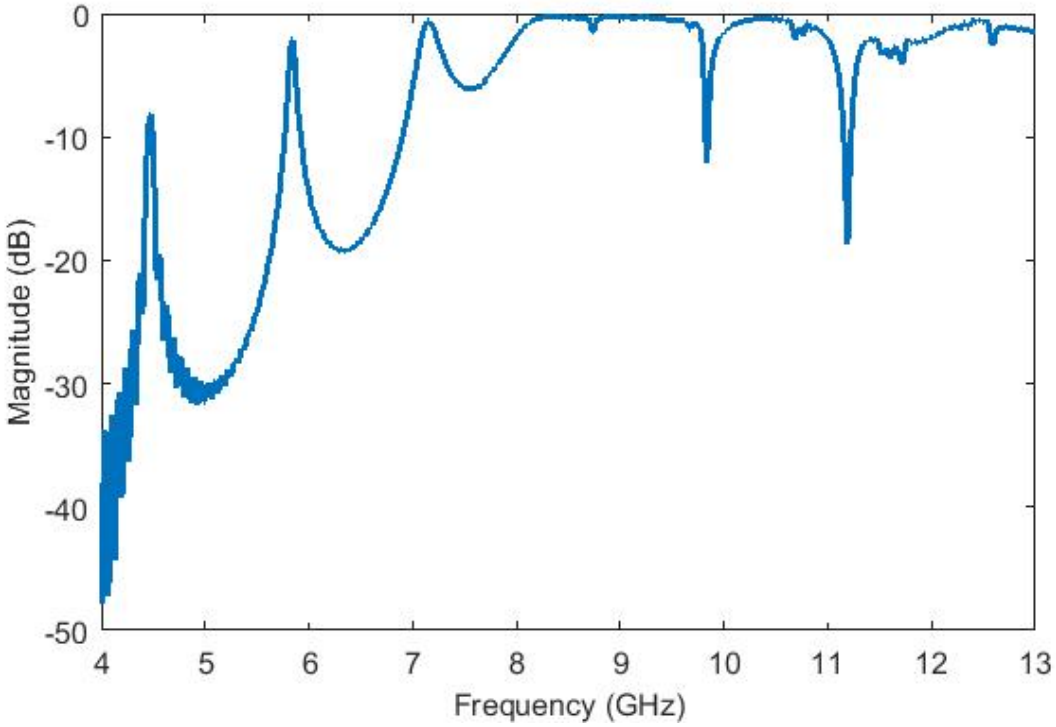

Fig. 14. S_{21} of ogee geometry process seal insert for waveguide-to-coax adapter.

All three geometries performed worse in simulation than an unfilled waveguide-to-coax adapter. The ogee geometry exhibited the least passband ripple, though it did have substantial nulls at 9.8 GHz and 11.2 GHz. The triangular geometry, on the other hand, had more nulls, but were not as deep. The elliptical geometry performed worst out of the three geometries with significant loss above 9 GHz. Though the simulation results showed positive notes for the triangular and ogive geometries, the MACOR still heavily impacted the waveguide-to-coax adapter's performance. Dielectric losses were lower than the total dielectric fill, but were still significant. The simulation results for dielectric losses at 10 GHz are shown in Table 2.

Table 2. Comparison of dielectric losses for different process seal insert geometries

Geometry	Dielectric Loss
Triangular	-13.857 dB
Elliptical	-14.529 dB
Ogee	-12.862 dB
Total Fill	-8.2862 dB

CST simulation models were stimulated with 0.5 W (-3.01 dB) of power. Dielectric loss was calculated as the difference between power accepted by the structure minus power output from all ports. Despite a dielectric loss reduction of 4.58 dB in the worst case (ogee versus total fill), the process seal insert geometries did not reduce the loss enough to function as a radiometer antenna. The dielectric losses would add to the noise temperature of the antenna which would decrease the radiometer sensitivity.

The last design of a process seal insert decreased the volumetric dielectric losses of MACOR by tapering the narrow wall of the waveguide. A standard waveguide-to-coax adapter was still used to excite the antenna. An additional component was added after the waveguide-to-coax adapter to taper the narrow wall from 0.4 in to 0.125 in. A cross-

section of the CST MWS model of the waveguide-to-coax adapter tapered to a small aperture filled with MACOR can be seen in Fig. 15.

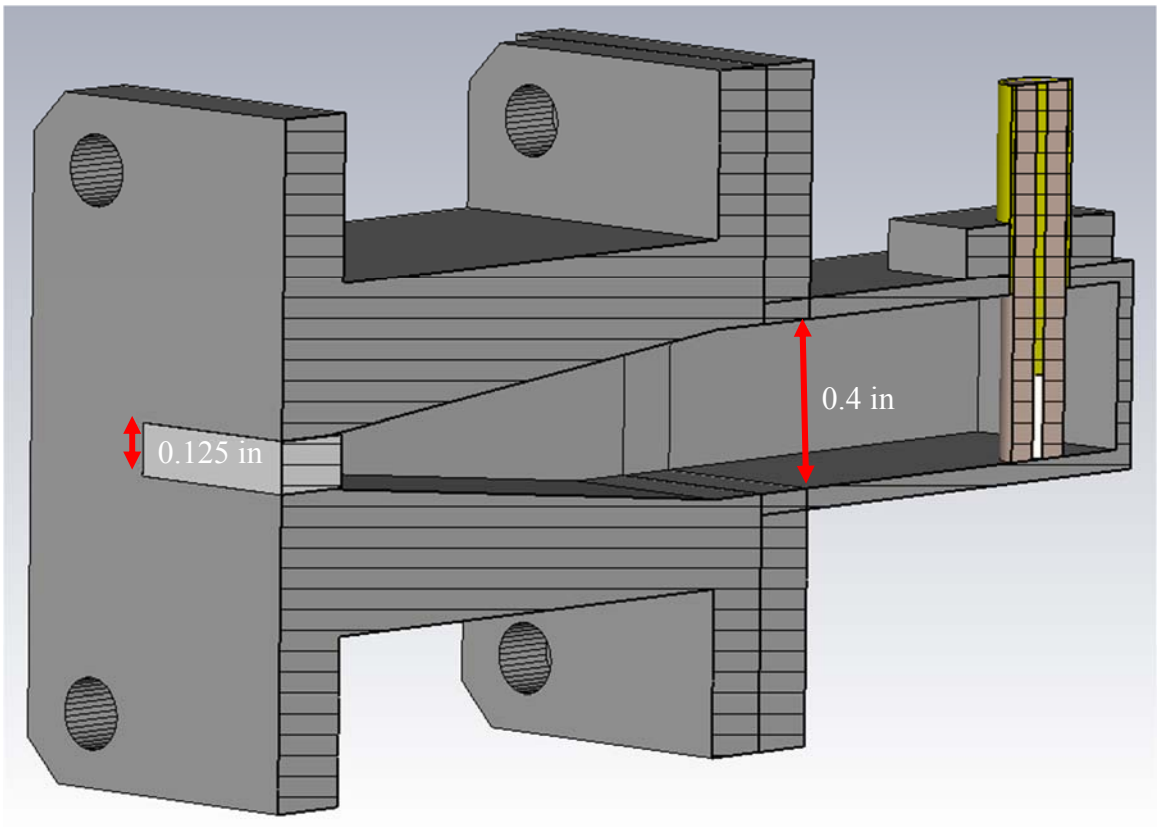

Fig. 15. Waveguide-to-coax adapter to taper section with MACOR.

One of the advantages of this design was the narrower aperture created a wider antenna beamwidth. Ice could then be detected in a larger area underneath the antenna, as opposed to a narrow swath underneath it. This design had the added benefit of reducing the total volume of MACOR needed to fill the adapter. A detailed mechanical drawing of just the taper section can be seen in Appendix A. Dimensions for the MACOR block were 0.9 in long, 0.125 in high, and 0.2 in thick. The results from an S-parameter simulation can be seen in Fig. 16.

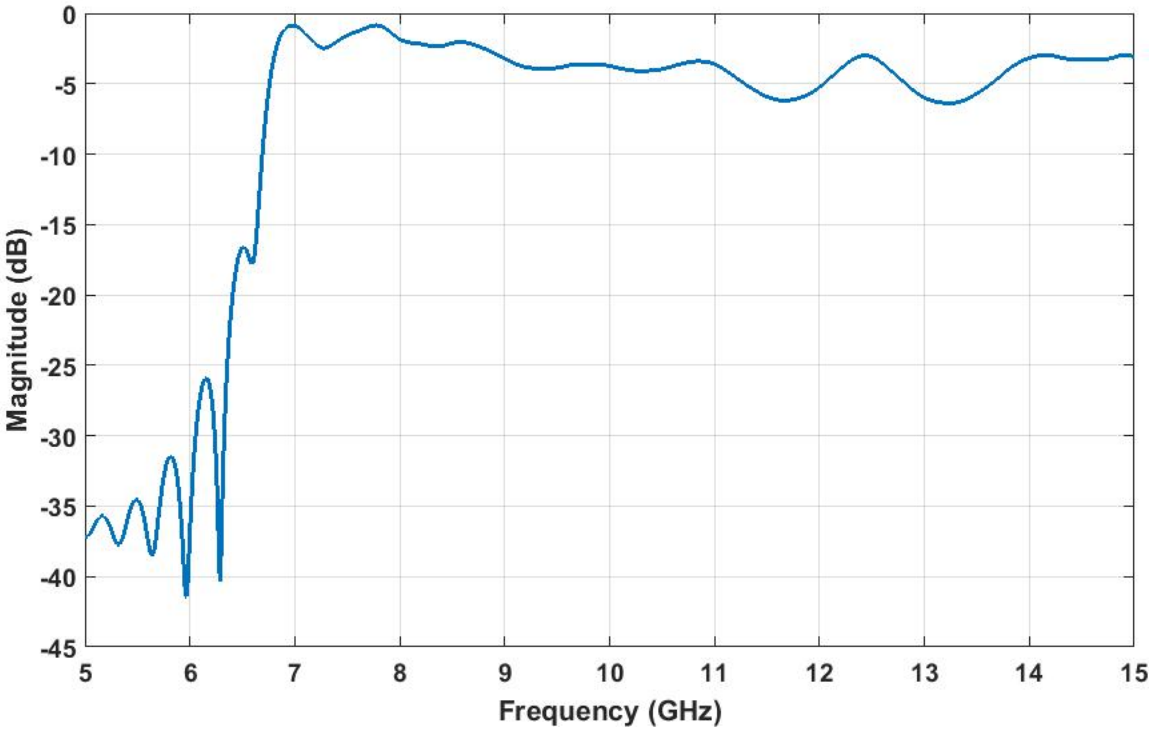

Fig. 16. S_{21} of tapered waveguide-to-coax adapter with MACOR process seal insert.

Despite the taper and the MACOR block, the cutoff characteristic of the waveguide-to-coax adapter was undisturbed. The combination of the taper and the MACOR did create some transmission loss as seen by the reduced S_{21} over the frequency band. The process seal insert was not the major contributor to that loss, however, because the calculated dielectric loss at 10 GHz was only -22.189 dB. This design showed superior dielectric loss performance compared to any of the three modified geometry process seal inserts. Tapering the narrow wall of the waveguide attenuated the signal, but not so much that the design was unusable.

There were several mechanical issues that would need to be resolved with this design before actual implementation. First, the antenna height was over two inches which would extend too far into other parts of a jet engine. Second, the MACOR block would need to be secured somehow to be able to handle external pressure. Both of these issues

could be addressed in a second phase design. To perform a proof of concept, a prototype waveguide section with a process seal insert was manufactured. A picture of the process seal insert prototype with a waveguide-to-coax adapter attached is shown in Fig. 17.

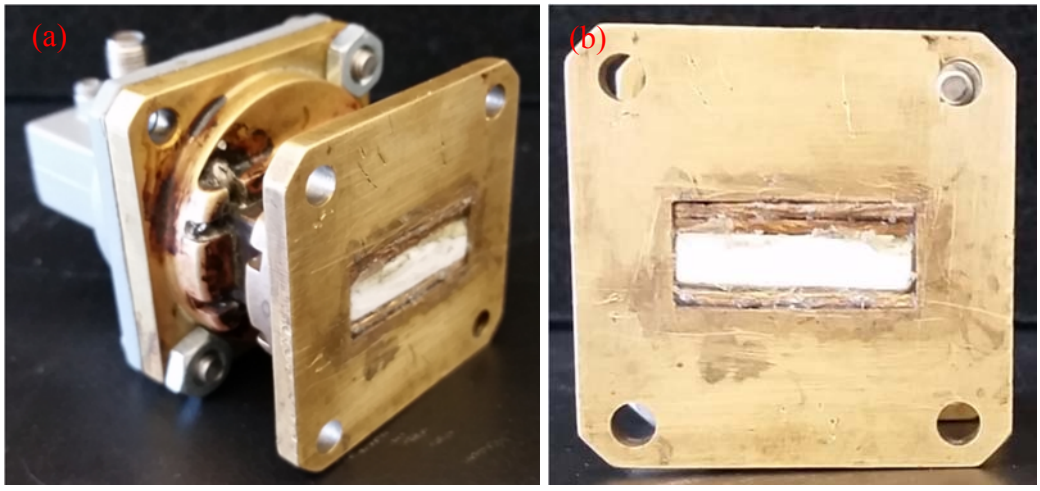

Fig. 17. Prototype process seal insert connected to waveguide-to-coax adapter. (a) Perspective view. (b) Front view.

The prototype had an abrupt transition from a narrow wall dimension of 0.4 in to 0.2 in, as opposed to a linear taper. The transition was made by stacking thin pieces of metal inside the waveguide and soldering them in place. A small MACOR block filled the remaining air cavity, and hot glue held the block to the metal. The dimensions of the MACOR block were 0.9 in wide, 0.2 in tall, and 0.38 in deep.

Planar Antenna Design

An alternative way to avoid the problem of the air cavity of a waveguide-to-coax adapter was to use a planar antenna instead. A planar antenna has the benefit of less extension into the jet engine bypass flow. The trade-off, however, with using a planar antenna was decreased bandwidth. A common definition of antenna bandwidth is the frequency range over which the antenna's $S_{11} < -10$ dB. Few planar antennas are able to

achieve the 4 GHz bandwidth of a WR-90 waveguide-to-coax adapter. Despite this, a planar antenna only needed to have a bandwidth greater than or equal to that of the microwave radiometer (1.2 GHz). A 1.2 GHz bandwidth was achievable using conventional planar antenna designs.

Two planar antenna designs, a microstrip patch antenna and a planar bowtie antenna, were modeled and simulated in CST MWS. These two designs were chosen because their designs are well-documented, and they are frequently used in microwave systems. The desired center frequency was 10 GHz with a 3 dB bandwidth of 1.2 GHz. The physical size of the antenna also needed to be smaller than the WR-90 aperture to be used with the stator vane assembly.

The first planar antenna design considered was the planar bowtie antenna. A planar bowtie antenna can be thought of as a wideband dipole antenna. Instead of using two wires like the dipole, a planar bowtie antenna's aperture fans out into two triangles. Fig. 18 shows a CST MWS model of a planar bowtie antenna.

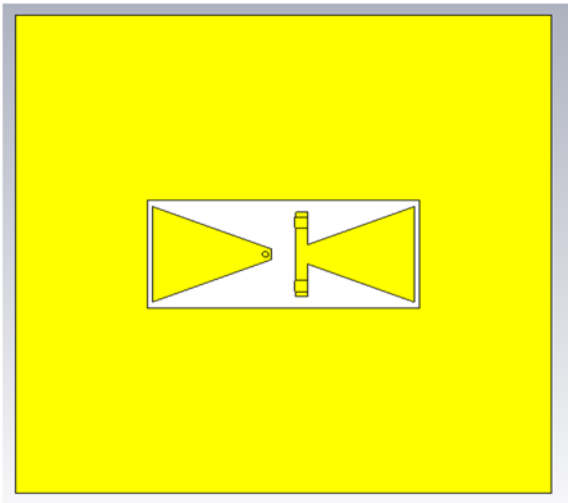

Fig. 18. CST MWS model of planar bowtie antenna on FR-4 substrate.

Though it is not shown, an SMA connector was fed through the backside of the board. The center pin connected to the left bowtie, and two of the grounding pins connected to the right bowtie. The board dimensions were 1.63 in by 1.63 in to match the size of a WR-90 flange. There are several modifications that have been made to a standard planar bowtie antenna design. First, there was a top layer of copper completely surrounding the antenna. Most planar antennas will have nothing else on the top layer besides the antenna itself. The reason for the additional copper was to model what the antenna would experience on the stator vane assembly. When the antenna was mounted to the stator vane assembly there was aluminum entirely surrounding the aperture, so it turned out to be easier to design the antenna with this in mind. Second, a grounding wall was placed around the antenna that connected the top and bottom board layers. In simulation, the grounding wall was an actual sheet of copper inserted into the board. In fabrication, the grounding wall was implemented by stitching wire through holes spaced closer than a half-wavelength apart. The purpose for the grounding wall was to electrically isolate the antenna from the rest of the board. The substrate would contribute to the antenna noise, so it was desirable to mitigate its effect. Antenna prototypes were printed on an FR-4 substrate which has considerable loss at high frequencies ($\tan \delta \approx 0.018$ at 10 GHz). Substrate loss was a concern because of its intended use with the microwave radiometer. The planar bowtie antenna was simulated in CST MWS from 5 to 15 GHz. The S-parameter simulation results for this antenna can be seen in Fig. 19.

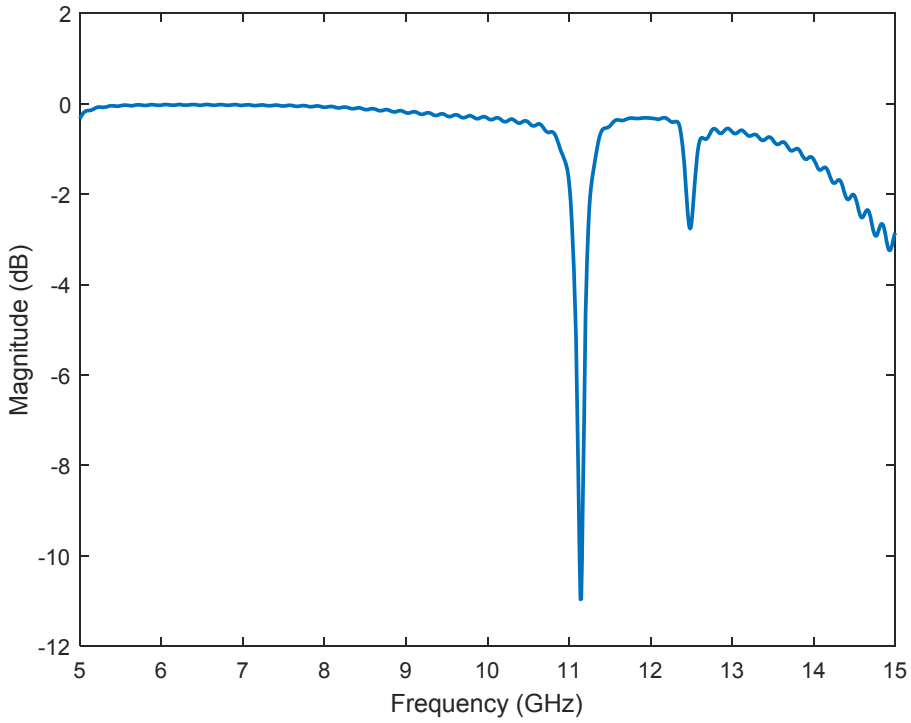

Fig. 19. S_{11} of planar bowtie antenna back-fed by SMA.

For a one-port device, like a planar antenna, only S_{11} can be calculated. S_{11} measures how much of the voltage wave exits port 1 that was input to port 1 [23, p. 559]. A null in the S_{11} of an antenna means that power was accepted by the structure for radiation. In Fig. 19, the null occurred at 11.14 GHz which is higher than the target center frequency of 10 GHz. Unfortunately the bowtie antenna could not be made larger to lower its center frequency due to size constraints. In addition, the close proximity of the top layer of copper prevented surface currents from flowing properly on the antenna, resulting in an uncharacteristic narrow bandwidth.

The second planar antenna design considered was the microstrip patch antenna. A microstrip patch antenna is smaller than a planar bowtie antenna designed for the same frequency, but sacrifices bandwidth. Fig. 20 shows a CST MWS model of a microstrip patch antenna used for S-parameter simulations.

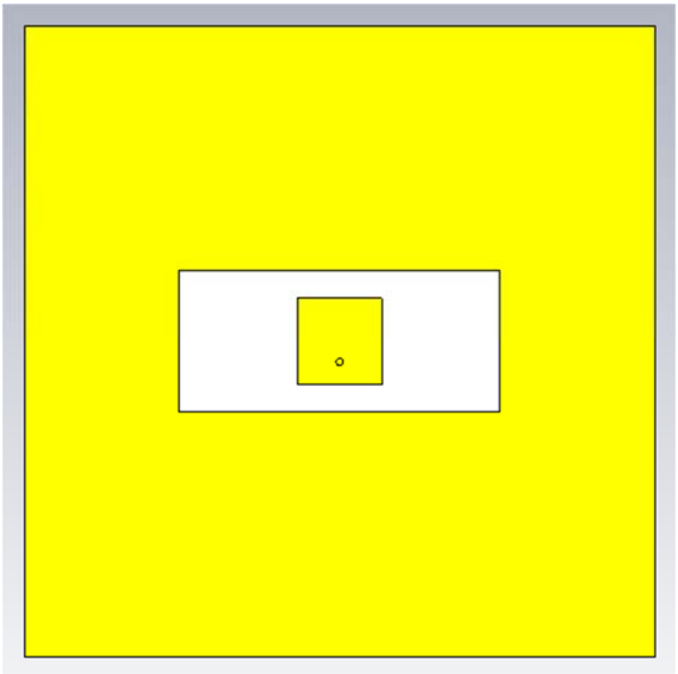

Fig. 20. CST MWS model of microstrip patch antenna back-fed by SMA.

The same modifications were made in designing the microstrip patch antenna for the stator vane assembly. The following design equation was used to determine the approximate antenna height for a center frequency of 10 GHz [24].

$$H=0.49*\frac{\lambda_0}{\sqrt{\varepsilon_r}} \tag{20}$$

The approximate wavelength at 10 GHz in free space is 3 cm, and FR-4 has a relative permittivity of 4.3. From (20), the necessary height of a microstrip patch antenna was 0.709 cm (or 0.279 in) which easily fits inside the WR-90 aperture. The bandwidth of a planar antenna increases with substrate thickness, but so do dielectric losses [25]. Nevertheless, the antenna was designed for a 59 mil thick FR-4 substrate. Like the planar bowtie antenna, the microstrip patch antenna was also simulated in CST MWS from 5 to 15 GHz. Simulation results can be seen in Fig. 21.

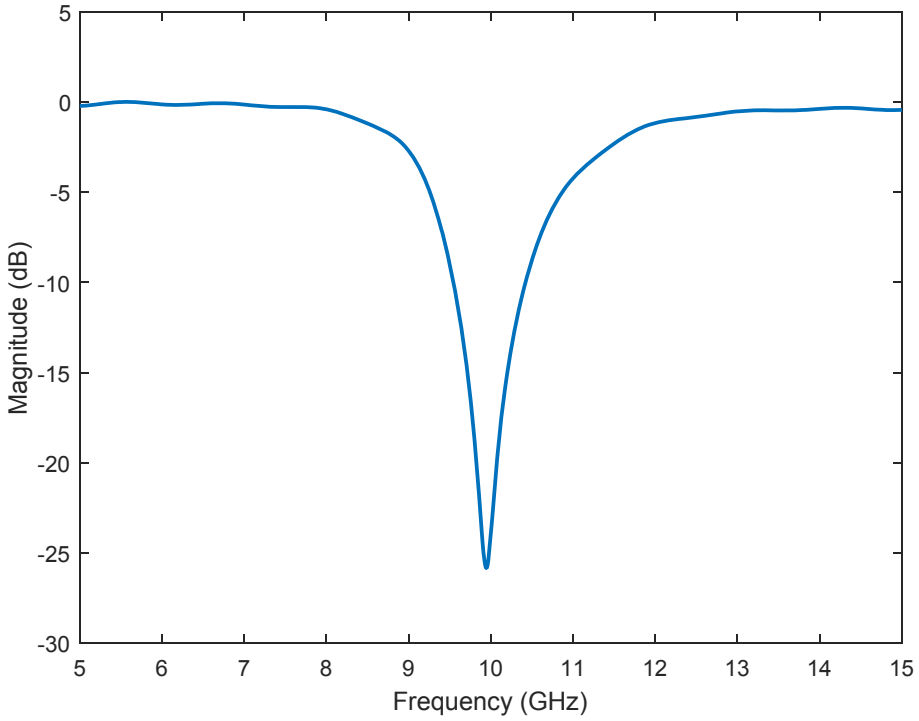

Fig. 21. S_{11} of microstrip patch antenna on FR-4 substrate

The S_{11} of the microstrip patch antenna clearly outperformed the planar bowtie antenna. This design was able to achieve a center frequency of 9.95 GHz with a bandwidth of 890 MHz (8.94%). A bandwidth of 1.2 GHz was the design goal, but 890 MHz was sufficient for a first pass. Despite the seemingly good antenna performance, the FR-4 substrate still was too lossy to use as a radiometer antenna. CST MWS stimulated the structure with 0.5 W of power, but 0.111 W was lost in the dielectric. The significant loss would cause antenna noise that prevents the radiometer from efficiently receiving the thermal radiation from the environment.

Rogers RO3003 high-frequency laminate was chosen as the new substrate for a low loss antenna design. Table 3 provides a side-by-side comparison of the important properties of FR-4 and RO3003.

Table 3. Comparison of material properties of FR-4 and RO3003 at 10 GHz.

Property	FR-4	RO3003
Dielectric Constant	4.3	3.00
Loss Tangent	0.018	0.001
Available Thickness	0.059 in	0.060 in

FR-4 has a loss tangent more than ten times greater than RO3003 making it a poor choice of substrate for a microwave radiometer antenna. The new calculated antenna height from (20) was 0.848 cm (or 0.334 in.) which was still smaller than the WR-90 aperture. Simulation results of the new microstrip patch antenna design can be seen in Fig. 22.

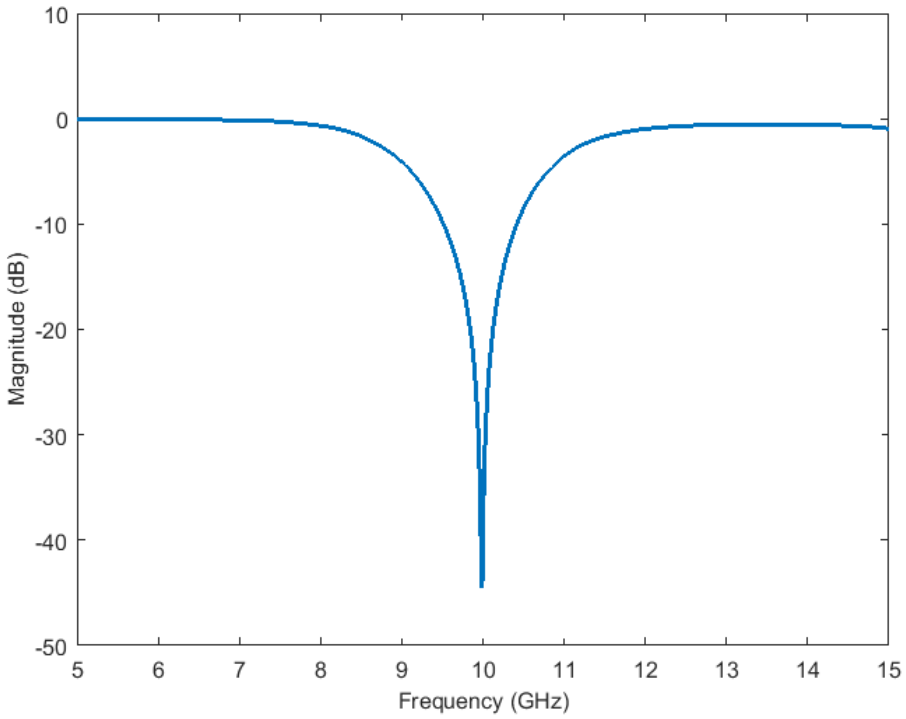

Fig. 22. S_{11} of microstrip patch antenna on Rogers RO3003 substrate.

A center frequency of 9.99 GHz was achieved with a bandwidth of 910 MHz in simulation which was very similar to the FR-4 design. Only 0.0041 W of power was lost

in the Rogers RO3003 substrate as compared to the 0.111 W lost in the FR-4 substrate. Both antenna designs were fabricated, and tested with the ice accretion sensor.

In a jet engine, there would need to be a dielectric window over the antenna as well for durability. This extra design feature was ignored for initial testing of the antenna designs. It would not be difficult, however, to implement a dielectric window later. The primary measurement environment considerations in this work were engine geometry and the need for a low-profile but high durability antenna. The stator vane assembly, process seal inserts for a waveguide-to-coax adapter, and planar antenna designs attempted to make the ice accretion sensor in-lab experiments as realistic as possible.

CHAPTER FOUR

Experimental Results

The following section shows data from in-lab testing of the ice accretion sensor. One of the main goals of the in-lab testing was to create a testing environment that would approximate the inside of a jet engine. This effort could only go so far, as the air speeds and pressures inside a jet engine were not able to be replicated in the lab. The temperature and geometry, however, were very similar to what the ice accretion sensor would experience in a real implementation. Initial results were obtained in an ideal measurement set-up to demonstrate the microwave radiometer's performance, and to determine what center frequency, or frequencies, should be used. The test set-up was gradually modified to take into account the measurement environment considerations. Results were ultimately obtained for ice accretion at different temperatures at a center frequency of 10 GHz.

Test Set-Up

To ensure the accuracy of measurement results, a consistent test set-up was needed. The size of the test set-up was not a concern in the lab, so data processing was done separate from the microwave radiometer. Fig. 23 shows the major components of the test set-up for the ice accretion sensor.

Fig. 23. Test set-up for ice accretion sensor. Numbered labels added to identify individual components.

The first component of the ice accretion sensor test set-up, labeled (1), was the microwave radiometer. A metal enclosure was used to isolate the microwave radiometer from errant signals that could disturb the measurement data. Polymer foam sheets insulated the inside of the enclosure so that the temperature would be stable inside. During experiments that referenced to a load inside the enclosure, it was very important to keep the enclosure at a stable temperature. Load temperature fluctuations during an experiment created inconsistency in the data. The electrical components inside the enclosure dissipated enough heat to warm the enclosure to approximately 36°C on their own. As long as the microwave radiometer reached a stable temperature before capturing data, no other temperature regulation was needed.

The second component in Fig. 23 was a Tenney TUJR environmental test chamber (ETC) where the radiometer antenna, and sometimes the reference load, were located. The Tenney ETC has a temperature range of -77°C to 150°C which was more than sufficient for the needs of this project. Data were mostly taken in the temperature

range of -10°C to 10°C to examine water (and consequently ice) around its freezing and melting point. Fig. 24 shows an example of connections to the stator vane assembly inside the Tenney ETC.

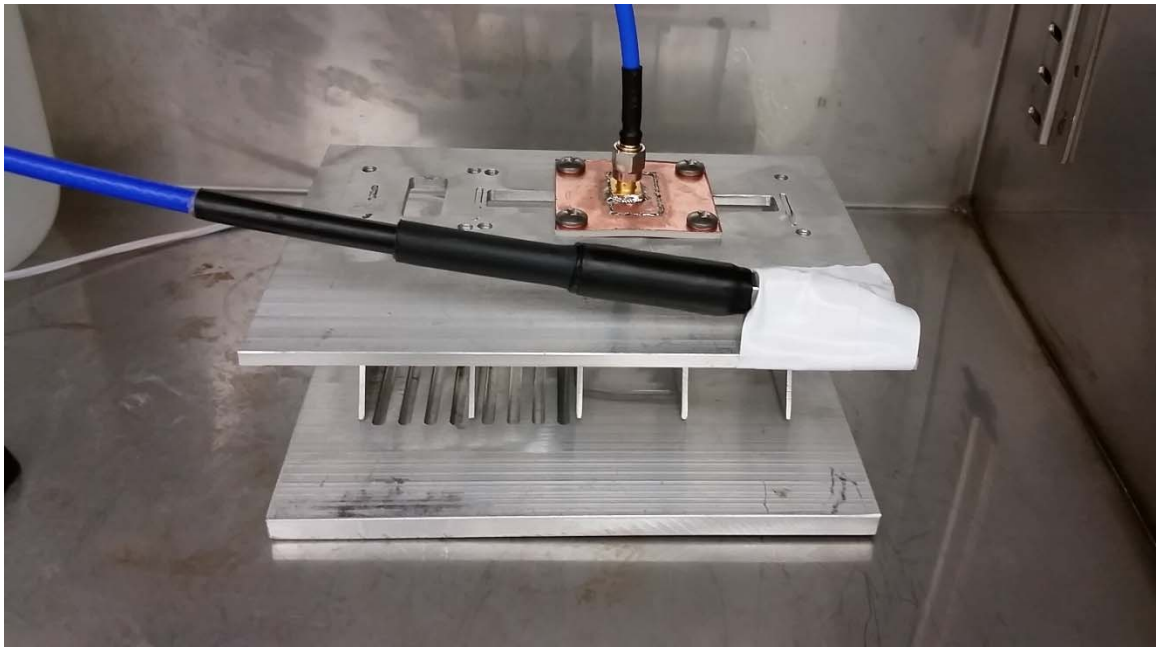

Fig. 24. Stator vane assembly inside ETC. Planar antenna and 50 Ω reference load connected.

The radiometer antenna in Fig. 24 was a planar antenna on a Rogers RO3003 substrate. The reference load was a 50 Ω termination that was taped to the stator vane assembly for thermal contact. During testing, there was also a webcam that took a picture of the stator vanes with each data capture. Data from this test set-up can be found later in this chapter.

The third component shown in Fig. 23 was the HP-8720ET VNA used as the microwave radiometer's LO. It should be noted that a smaller oscillator, such as a dielectric resonant oscillator or YIG oscillator, could be used in future design iterations. The output from the LO connected to the frequency mixer inside the radiometer

enclosure. The fourth component was the LeCroy HDO4508 oscilloscope. The oscilloscope received inputs from the microwave radiometer, a resistance temperature detector (RTD) probe, and a function generator (component 5 in Fig. 23). An oscilloscope was included in the test set-up because it gave visual confirmation of the radiometer's operation. It also had a built-in averaging function for pre-processing the radiometer data. An example of the microwave radiometer output to the oscilloscope is shown in Fig. 25.

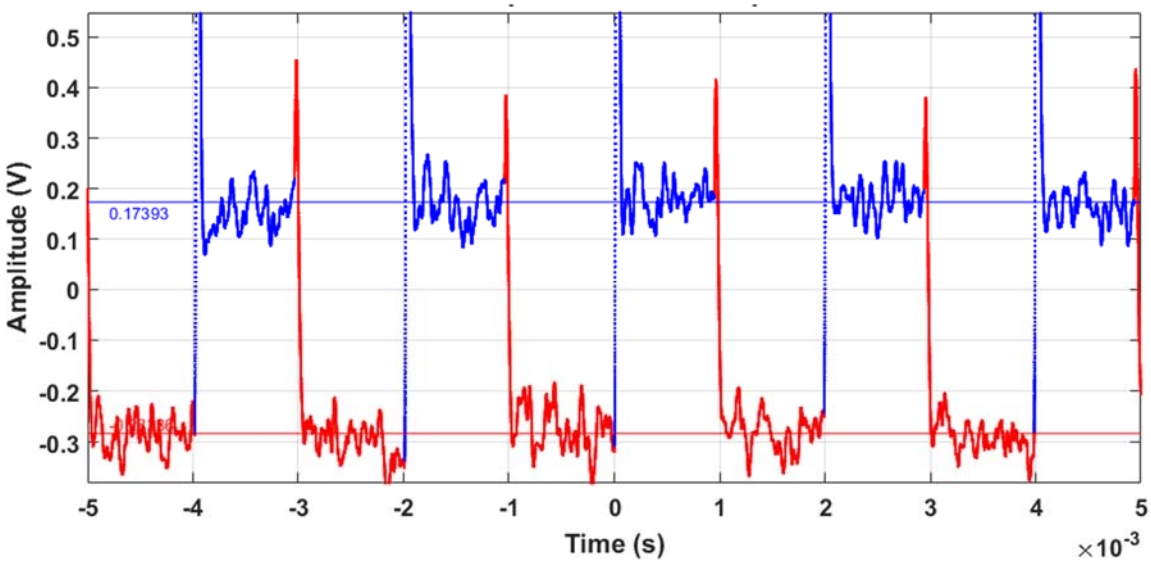

Fig. 25. Example radiometer output for one data capture as seen on the oscilloscope.

The data capture shown in Fig. 25 was averaged over 100 sweeps. Blue traces were the output voltage levels from the reference load, and red traces were the output voltage levels from the radiometer antenna. Switching between positive and negative voltages was a result of AC coupling. The time window for a single sweep on the oscilloscope was 10 ms. With a Dicke switching frequency of 500 Hz, the oscilloscope captured five voltages for both the radiometer antenna and reference load with each sweep. An average was calculated over the entire data capture for the antenna and

reference voltages (shown in Fig. 25 as the solid blue and red horizontal lines). The difference between these two averages was recorded, time-stamped, and paired with its corresponding temperature data. Typical data acquisition time for a single data point of differential voltage amplitude was 20 seconds. Speed of acquisition could be increased with an embedded processor inside the radiometer.

The sixth component was a DC power supply which provided 5 V to an RTD probe inside the ETC. Temperature data from the RTD probe were collected and averaged in the same way as the radiometer output. The seventh component was a Fluke 52 II digital thermometer. A probe from the digital thermometer was connected to the reference load. Data from the digital thermometer was not saved or transferred to the computer. Its purpose was to verify that the reference load was at a stable temperature during the experiments.

Initial Results

The first microwave radiometer experiment checked if the system could track the physical temperature of an object. An SMA 50 Ω termination was inserted in a beaker of water inside the ETC and connected to the microwave radiometer RF input. The ETC started at a temperature of 0°C, and increased the temperature by 10°C every 10 minutes until it reached 80°C. Water temperatures were expected to lag behind the ETC temperature. Center frequencies of 6 GHz, 10 GHz, and 14 GHz were used to test the multi-frequency capability of the microwave radiometer. The 50 Ω reference load was connected inside the radiometer enclosure. A plot of voltage versus temperature for the three center frequencies can be seen in Fig. 26.

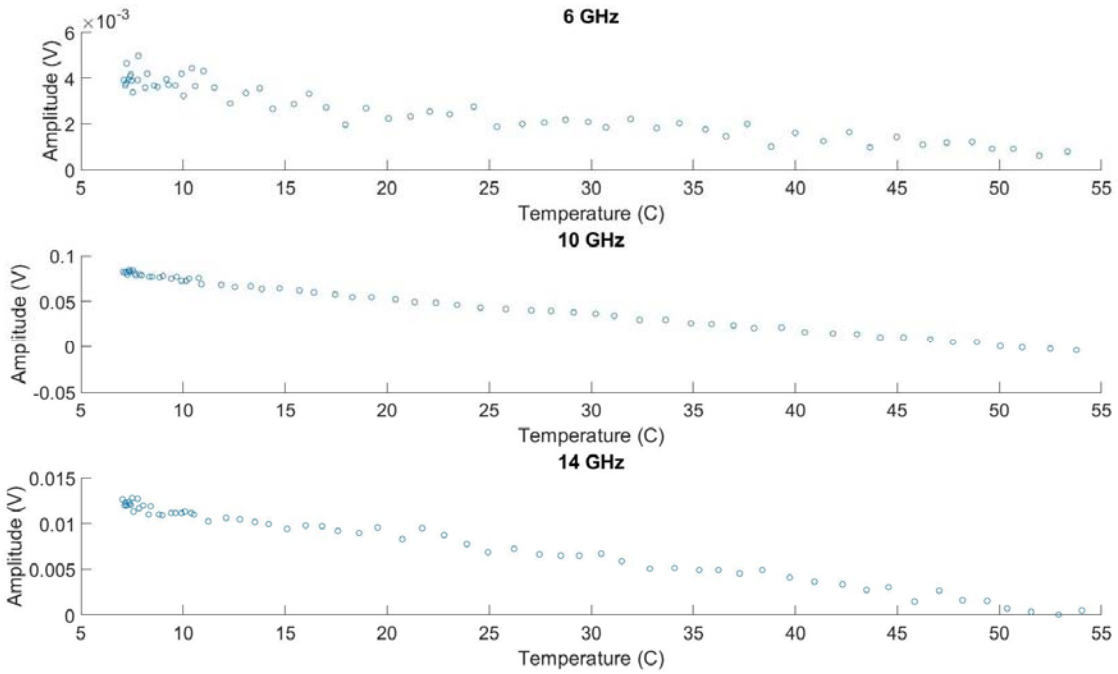

Fig. 26. Voltage vs temperature plots for water validation experiment.

At each center frequency, the microwave radiometer was responsive to the temperature change of the 50 Ω termination. As the physical temperature rose inside the ETC, the voltage amplitudes dropped. Keeping in mind the voltage amplitudes were actually a differential voltage between the radiometer antenna and the reference load, this phenomenon matched expectations. When the experiment began, the water was at 7°C whereas the reference load was at 36°C. The water temperature rose steadily throughout the experiment which decreased the difference between the antenna and reference brightness temperatures. If both the radiometer antenna and reference load had the same brightness temperature, there would be no voltage difference between them. Towards the end of this experiment, the voltage amplitudes were approaching this state.

The center frequency of 10 GHz exhibited the largest voltage range meaning it was the most sensitive to the temperature change. The data at 6 GHz and 14 GHz still

showed the same trend, but not as definitively. It should be noted that a center frequency of 6 GHz was below the lowest operating frequency of the frequency mixer. In addition, the reference load was only rated to 8 GHz, which could explain the poor performance at 14 GHz. As aforementioned, 10 GHz was identified as a candidate for a good choice of center frequency. The reference load seemed to be stable enough to use at 10 GHz despite its nominal operating frequency range. An analysis of the results from the water validation experiment showed that the microwave radiometer was operating as expected.

The next experiment that was performed used a WR-90 waveguide-to-coax adapter as the radiometer antenna. The antenna was connected to the stator vane test assembly inside the ETC. An alternative antenna, or at least a modified waveguide-to-coax adapter, would have to be used in a real implementation. The electric field polarization was perpendicular to the stator vanes. This experiment's goal was to observe how water and ice change the sensor's response on the stator vane assembly. The ETC temperature started at 0°C with dry vanes. After approximately 10 minutes, 5 mL of near 0°C distilled water was inserted in the passage where the antenna was focused. At the 20 minute mark, the ETC temperature was lowered to -10°C where it was held for 30 minutes to freeze the water between the vanes. The total experiment time was 50 minutes. Center frequencies of 10 GHz and 17 GHz were measured, though only 10 GHz yielded useful data. 17 GHz approaches the highest operating frequency of an SMA cable, so cable loss was a big contributor to the poor results. A plot of the differential voltage versus time at 10 GHz can be seen in Fig. 27.

An offset was removed by subtracting the average of the first ten minutes of data from the voltages. All data plots were normalized like this to remove the day-to-day

fluctuations of ambient temperature, humidity, etc. The different phases of water were determined by looking at pictures of the test set-up before plotting the data. Pictures of different stages from this experiment can be seen in Fig. 28.

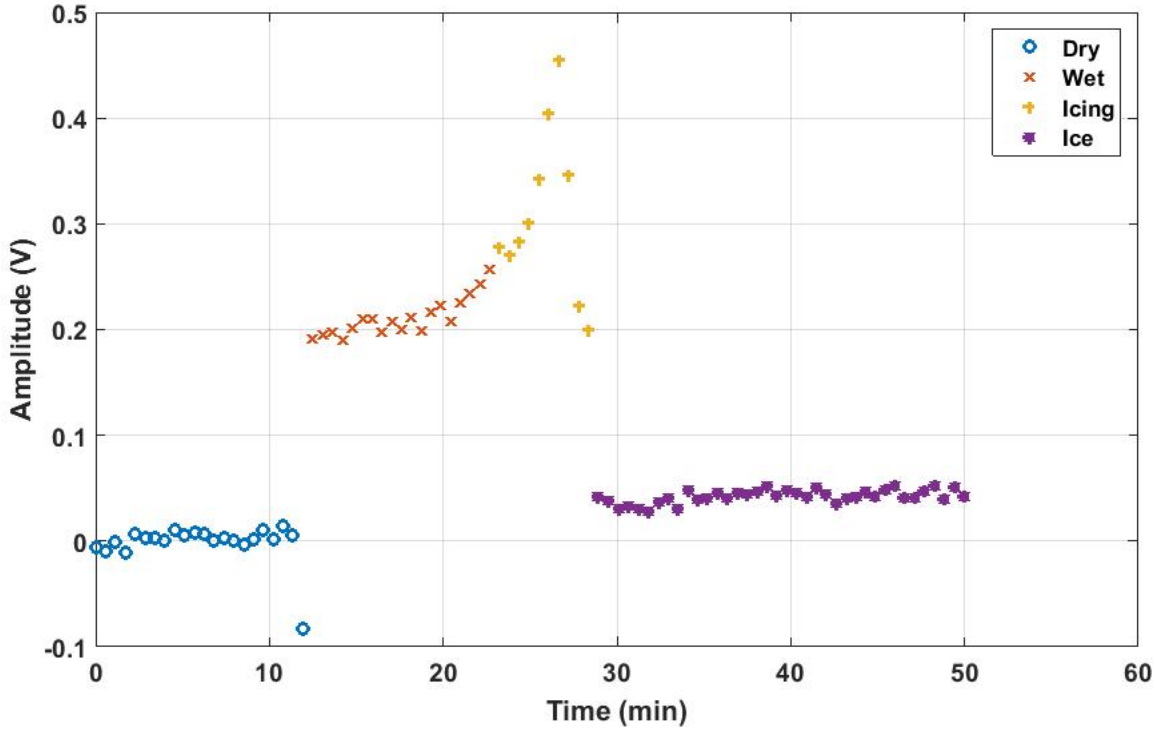

Fig. 27. Voltage vs time plot for water to ice experiment.

Fig. 28. Stator vane assembly at different stages during an experiment. (a) Dry vanes. (b) Wet vanes (5 mL of water). (c) Icing vanes. (d) Iced vanes.

At the 12 minute mark, there was a clear jump in the voltage amplitude caused by the cold water. Just like the water validation experiment, an increased voltage equaled a

decrease in antenna brightness temperature. Distilled water was therefore determined to have a lower emissivity than the aluminum of the stator vane assembly. At the 20 minute mark, when the ETC temperature dropped to -10°C, the amplitude increased briefly before dropping again as the water completely froze. The brief increase was caused by the temperature of the water dropping to 0°C before beginning its phase change. Although the ETC was set to 0°C, the temperature actually fluctuated by about ±2.5°C. As a result, the cold distilled water temperature rested around 2°C until the ETC temperature dropped to -10°C. By minute 28, the water had completely frozen. Ice between the stator vanes decreased the amplitude close to where it was with the dry vanes at 0°C.

Another experiment was conducted using the WR-90 waveguide-to-coax adapter as the radiometer antenna. The temperature profile of the ETC was the same as the previous experiment. The procedure was executed three times. First, the experiment was run with no water (i.e. a dry run). Second, 3 mL of water was added 10 minutes into the experiment. Third, 5 mL of water was added 10 mL of water was added at the 10 minute mark. Another difference from the previous experiment was the location of the radiometer reference load. For this experiment, the reference load was located outside the radiometer enclosure at room temperature. The conjecture was the room temperature would still be warmer than inside the ETC, but would also fluctuate less than the temperature inside the radiometer enclosure. The insulating foam inside the radiometer enclosure was not sufficient to maintain thermal equilibrium. Executing the procedure three times, and changing the location of the reference load were changes brought about

the shortcomings of the previous experiment. The 10 GHz results from this experiment can be seen in Fig. 29.

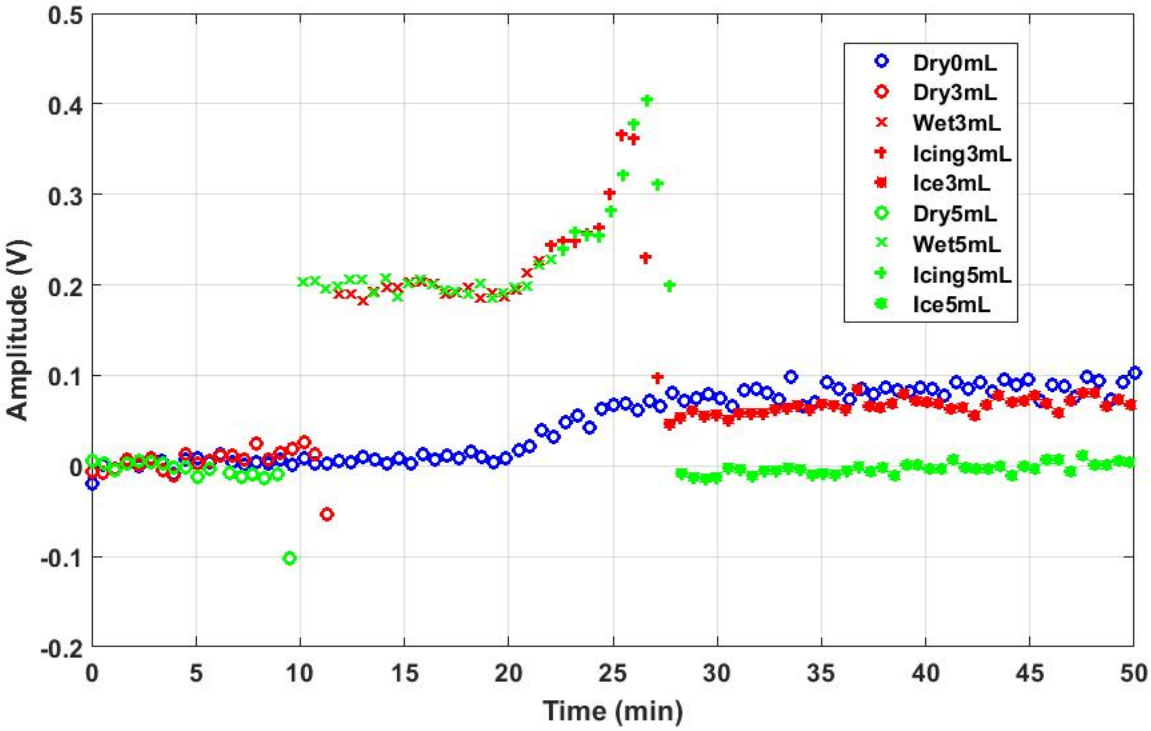

Fig. 29. Voltage vs time plot for water to ice experiment at different volumes. Tests ran with 0 mL, 3 mL, and 5 mL of distilled water.

Similar to the results from the previous experiment, an offset was removed from each data set. The data from the dry run (blue circles in Fig. 29) matched expectations in that the differential amplitude increased (antenna brightness temperature decreased) when the temperature dropped from 0°C to -10°C. Water was added at roughly the 10 minute mark which was clearly visible from the data. Both the 3 mL and 5 mL data sets exhibited a single data point drop below the normal amplitude for dry vanes just before water was added. The ETC was held at 0°C for the first twenty minutes of the experiment, but the door had to be opened to insert the water between the vanes. In doing

so, warm air from outside the ETC raised the temperature which decreased the amplitude momentarily.

Interestingly, the different volumes of water did not register a significant difference in amplitude from the sensor. Once the water froze, the two volumes could easily be distinguished. More importantly, there was a difference between the amplitudes of dry vanes and ice at -10°C. The difference was more pronounced between dry vanes and 5 mL of ice than dry vanes and 3 mL of ice as expected. This test confirmed the idea established in the previous experiment that both the aluminum and ice have higher emissivities than water. It also showed there was a measurable difference between dry vanes and ice at -10°C. What this data lacked, however, was a phase change from ice back to water.

A final experiment was conducted with the un-filled waveguide-to-coax adapter as the radiometer antenna. The purpose of this experiment was to show the full cycle of water freezing and melting again on the stator vanes. A third phase was added to the temperature profile of the ETC to melt the ice. The complete temperature profile for this experiment was 20 minutes at 0°C, 30 minutes at -10°C, and 30 minutes at 10°C. Instead of keeping the reference load at room temperature, the load was placed back inside the radiometer enclosure. Moving between these two locations did not have a significant impact because the reference load was at a stable temperature, and appeared brighter than the radiometer antenna at all times during the experiments. Center frequencies of 10 GHz and 15 GHz were chosen for this experiment. Plots of voltage versus time for 10 GHz and 15 GHz can be seen in Fig. 30 and Fig. 31.

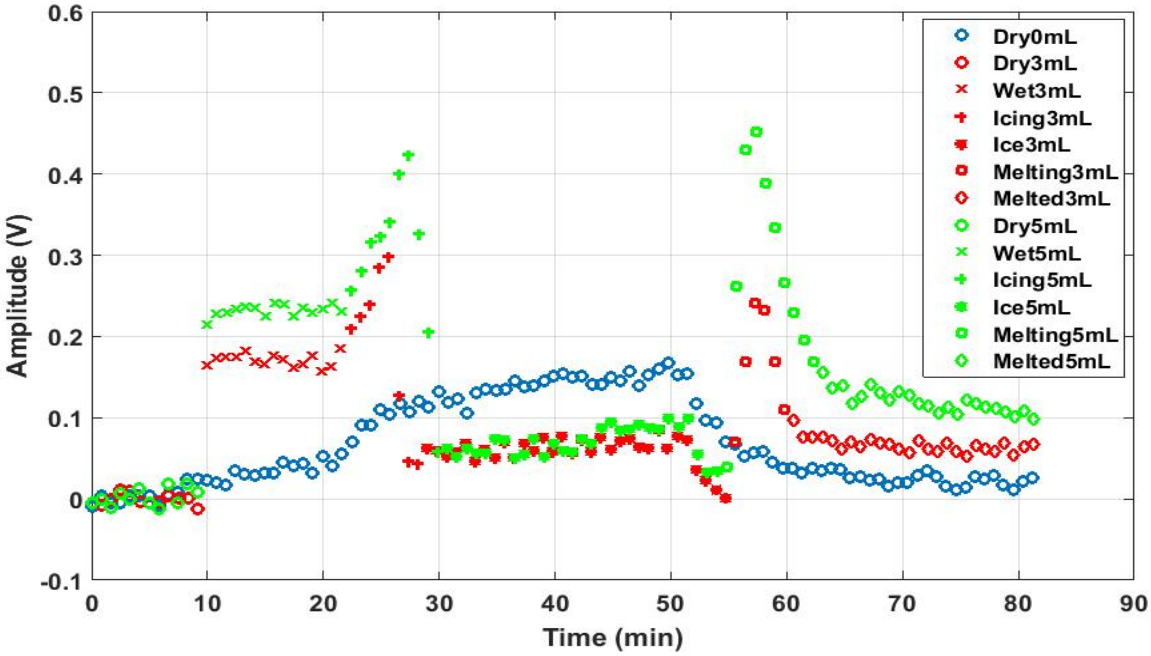

Fig. 30. Voltage vs time plot at 10 GHz for water to ice to water experiment at different volumes.

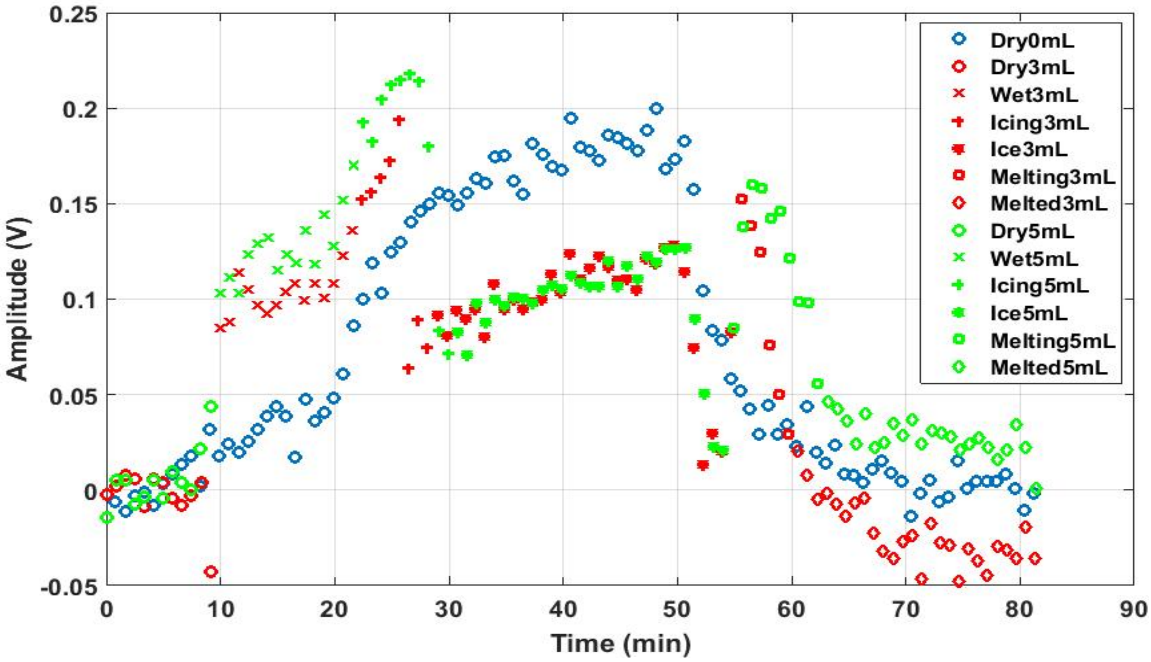

Fig. 31. Voltage vs time plot at 15 GHz for water to ice to water experiment at different volumes.

Amplitudes at 10 GHz were about twice as high as those at 15 GHz meaning about twice as much energy was received by the antenna at 10 GHz. Part of the decrease

in amplitude at 15 GHz may have been caused by SMA cable losses. In both plots, however, the addition of water at the 10 minute mark was clear. The difference between 3 mL and 5 mL of water was more evident from the 10 GHz data. Ice appeared brighter than the dry vanes at -10°C as expected, though the volumes could not be identified independently. After thawing, the different volumes of water were distinguishable only at 10 GHz.

One aspect of these results that did not meet expectations was the amplitude of the dry vanes at 10°C. An object's brightness temperature is proportional to its physical temperature, so the dry vanes at 10°C should have appeared brighter than the dry vanes at 0°C. A possible reason for this discrepancy was a fluctuation in the reference load temperature. If the reference load got hotter during the experiment, this could account for the dry vanes not appearing brighter at a warmer temperature. The results from this experiment illustrated the importance of having a temperature stable reference load. Overall, this experiment demonstrated the ice accretion sensor's ability to make the distinction between dry conditions, water, and ice with an un-filled waveguide-to-coax adapter. To further demonstrate the sensor's performance, experiments were performed with antennas that could be more readily implemented.

Process Seal Insert Results

The first experiment performed with a process seal insert was with a total fill of a WR-90 waveguide-to-coax adapter as the radiometer antenna. It was acknowledged before the experiment that a total dielectric fill of a waveguide-to-coax adapter with no re-design would probably not yield usable results. The S-parameters of the totally filled waveguide-to-coax adapter were not promising. This experiment was meant to be used as

a baseline to compare the results of experiments run with other process seal insert designs. Also, this experiment could provide information about the emissivity of MACOR. The temperature profile for the ETC was the same as the previous experiment with the un-filled waveguide-to-coax adapter. A center frequency of 10 GHz and 12.5 GHz was used during this experiment instead of 10 and 15 GHz. 15 GHz is approaching the cutoff frequency of the fundamental mode of SMA cables, so 12.5 GHz and lower is preferred. Results of voltage versus time at 10 GHz and 12.5 GHz are shown in Fig. 32 and Fig. 33.

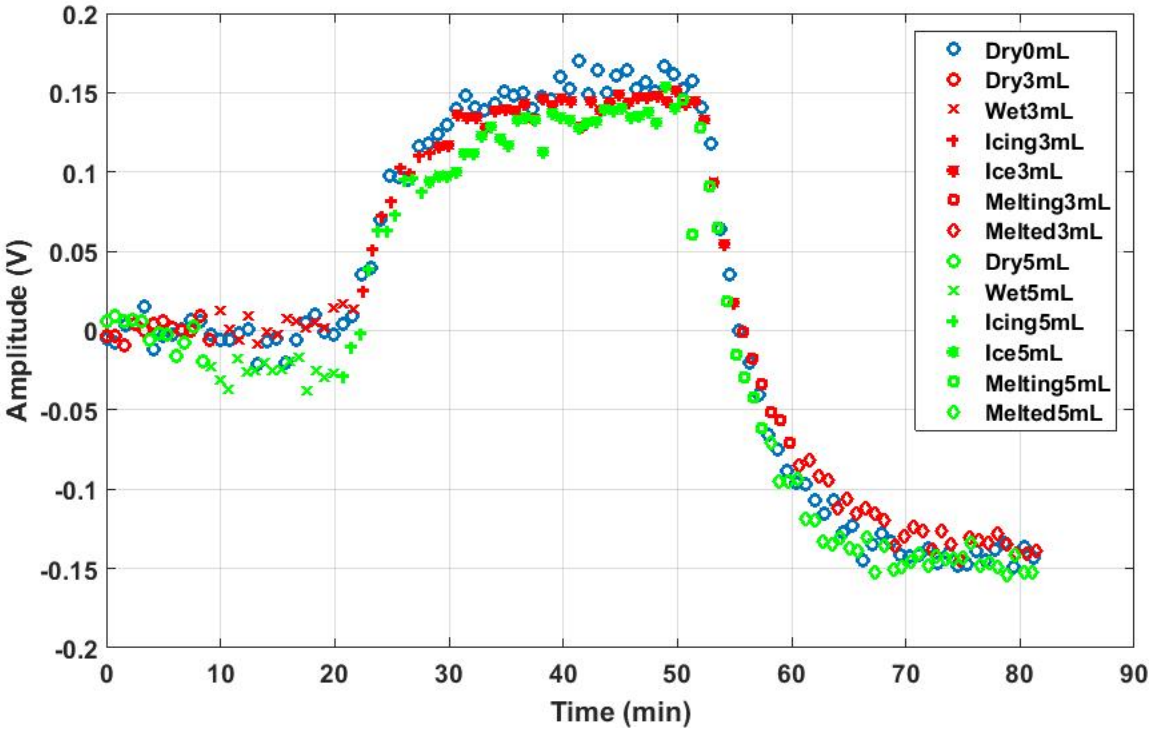

Fig. 32. Voltage vs time plot at 10 GHz for total fill of waveguide-to-coax adapter.

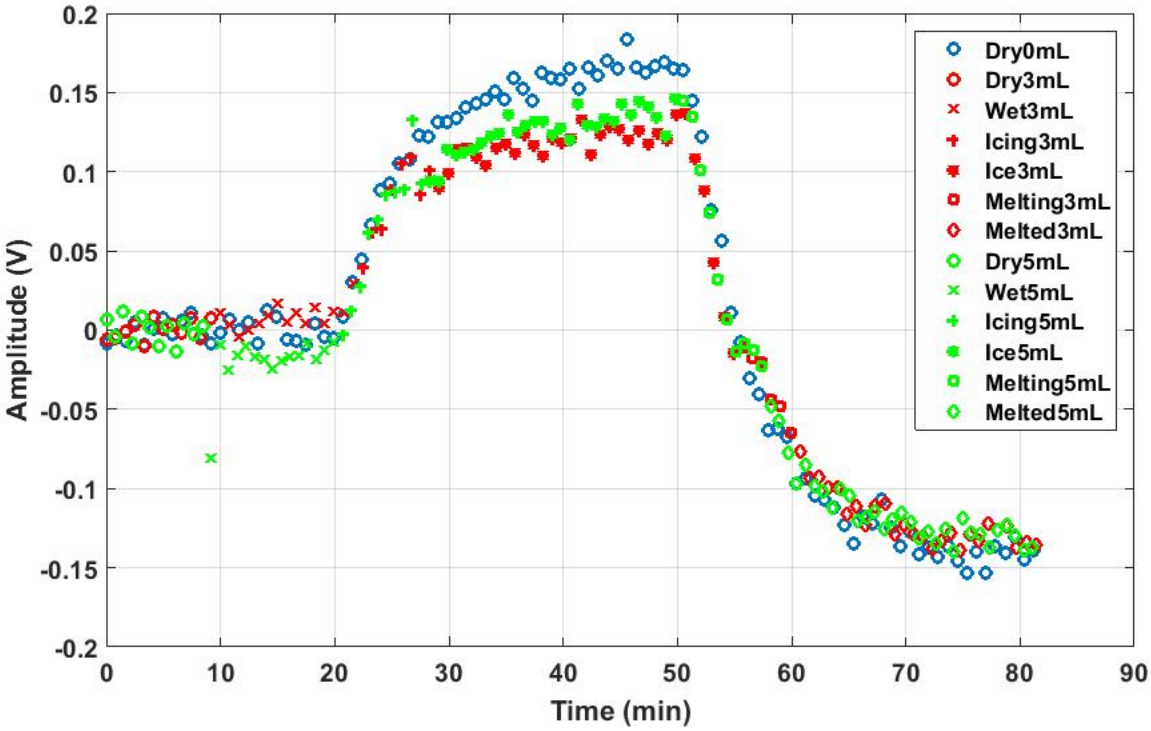

Fig. 33. Voltage vs time plot at 12.5 GHz for total fill of waveguide-to-coax adapter.

The MACOR fill caused the radiometer to lose its sensitivity to liquid water. Unfortunately, it also significantly dulled the radiometer's sensitivity to ice. Ice was somewhat detectable at 12.5 GHz, but not to the same degree as with the un-filled waveguide-to-coax adapter. The observed changes in amplitude over time were created by the temperature change of the MACOR itself. Dielectric losses and impedance mismatch were undoubtedly two large contributors to the poor performance. MACOR is believed to have a low emissivity because of the large offset removed from the data, and its reflective surface. If a process seal insert were to be used to fill a waveguide-to-coax adapter, a total dielectric fill was not a viable option.

Given the poor results with the total fill process seal insert, another experiment was performed with the prototype process seal insert. The reference load was located inside the ETC, and a single center frequency of 10 GHz was used. The data acquisition

speed was doubled from the total fill experiment because only one center frequency was used. Voltage versus time results can be seen in Fig. 34.

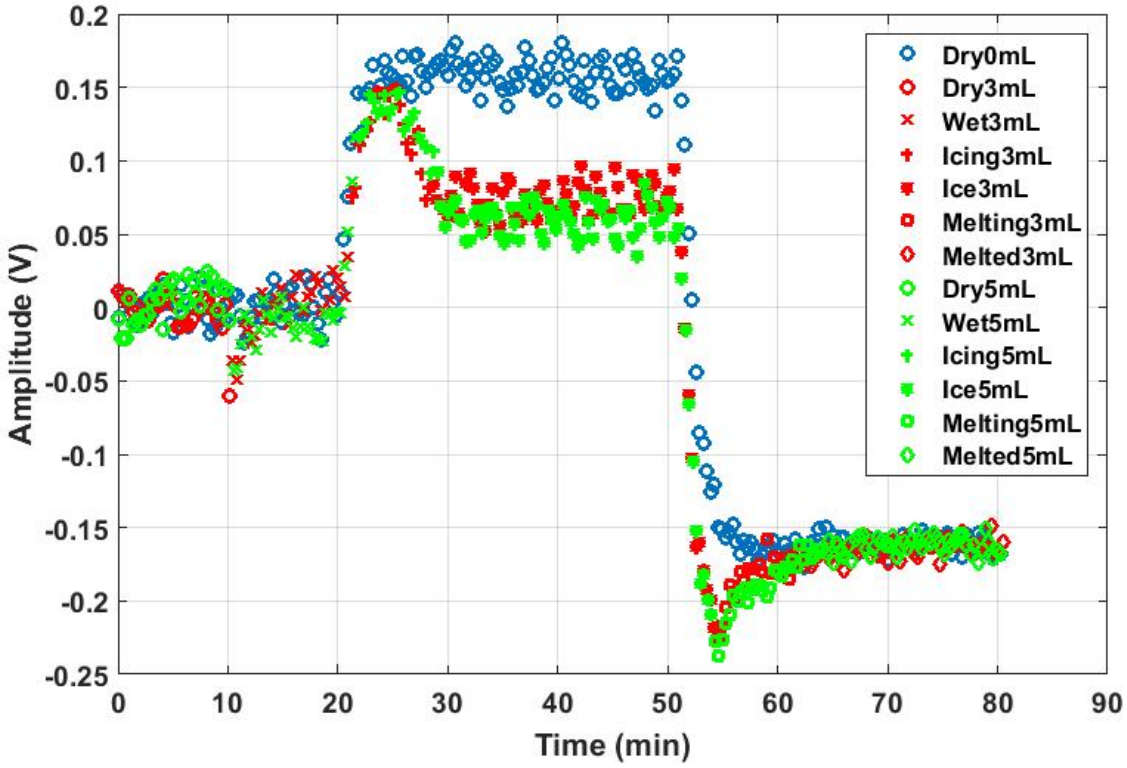

Fig. 34. Voltage vs time plot at 10 GHz for prototype process seal insert.

The first thing to note about the results was the lack of sensitivity to water. Not being able to sense the addition of water was consistent with the total dielectric fill of the waveguide-to-coax adapter. Two brief spikes around the 10 minute mark were caused by the opening of the ETC to insert the water. Even though the door was only open for about thirty seconds, the chamber temperature climbed by several degrees. Water was not visible from the sensor response once the ETC temperature settled again. After the 60 minute mark, when the ice completely melted, water was again indistinguishable from the dry run. MACOR is a lossy dielectric, so the emissions from the water may have been attenuated through the process seal insert below the detection threshold of the system.

The second thing to note was a sensitive response to ice even through the process seal insert. As the ice began to freeze, roughly from minute 20 to minute 30, the response began to deviate from the dry run. Once the ice completely froze, its amplitude was completely distinguishable from the dry amplitude. The amplitude differences between volumes of ice and dry were just as large as with the un-filled waveguide-to-coax adapter. Another experiment was performed with the prototype process seal insert to make sure the results were consistent. The reference load was located inside the ETC, and only 10 GHz was used as the center frequency. Up to this point, data had only been collected for ice at one temperature, -10°C. As a result, the temperature profile for this experiment was changed to 0°C for 10 minutes, -10°C for 20 minutes, and -20°C for 20 minutes. Voltage versus temperature results can be seen in Fig. 35.

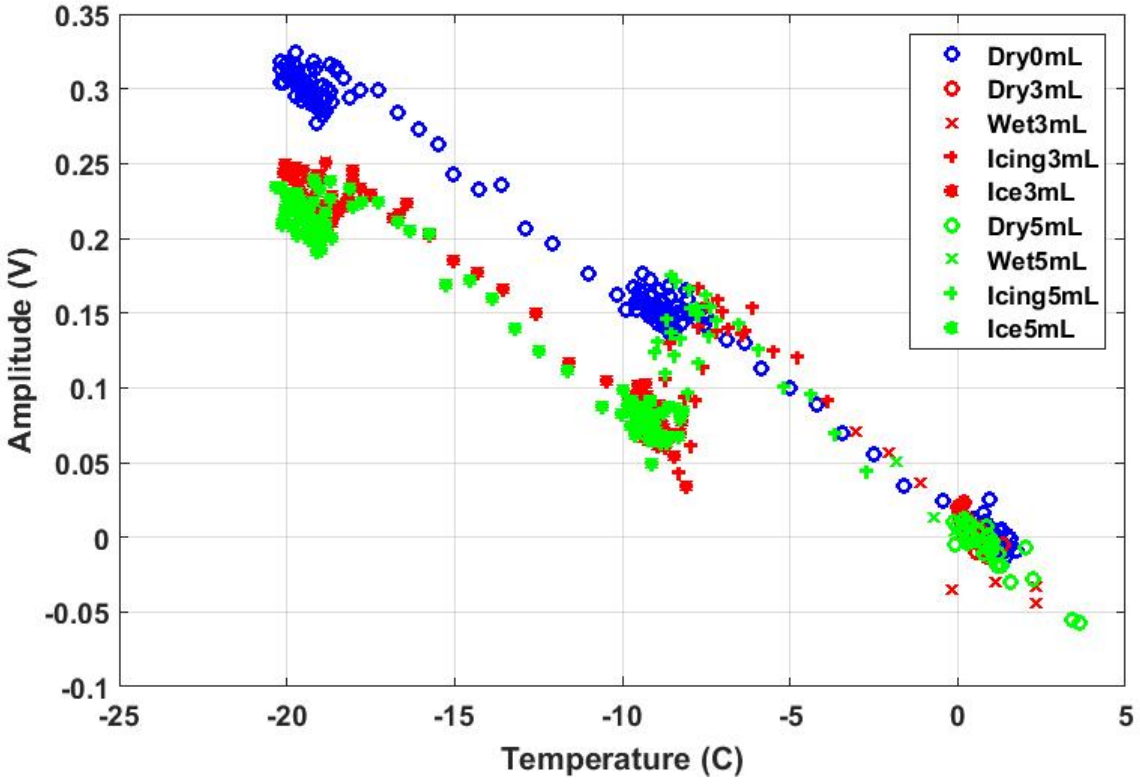

Fig. 35. Voltage vs temperature plot for prototype process seal insert.

Ice was still clearly distinguishable at -10°C and -20°C. Water was also not visible from the sensor response until it froze, like in the previous experiment. In a real scenario, however, the sensor would need to detect ice near 0°C. A third experiment was performed with the prototype process seal insert to detect ice accretion at more temperatures. The ETC temperature profile started at 0°C, then dropped to -15°C after ten minutes. After 20 minutes, the ETC temperature raised by 2.5°C until it reached 5°C. Voltage versus temperature results can be seen in Fig. 35.

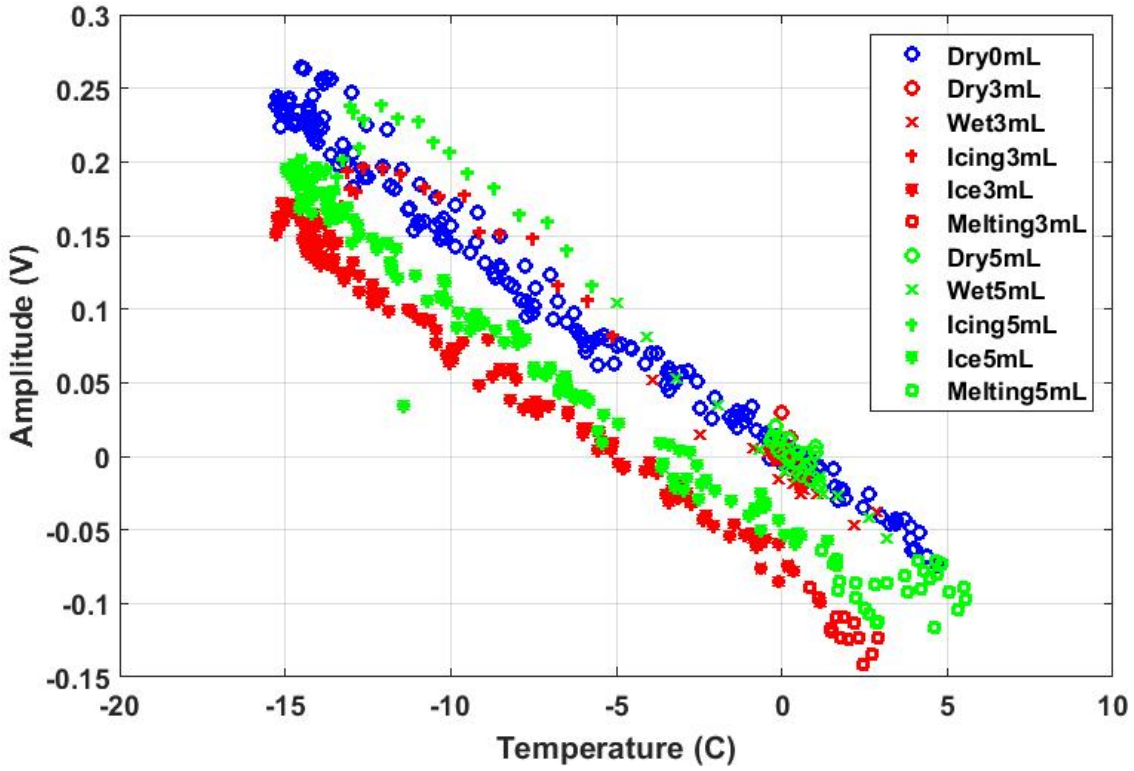

Fig. 36. Voltage vs temperature plot for prototype process seal insert.

A clear distinction could be made between dry and iced vanes. Most importantly, the ice at 0°C gave a different response than the dry vanes at 0°C. Even though 3 mL and 5 mL did not line up as expected, both are still distinguishable from the dry run. During the prototype process seal insert experiments, iced vanes had a lower amplitude

difference than dry vanes. The lower amplitude due to the presence of ice was consistent with the results from the un-filled waveguide-to-coax adapter. From a physical interpretation, ice made the antenna brighter due to its high emissivity which decreased the amplitude difference between the reference load and the antenna. The lack of sensitivity to water was ultimately a good result because the ice accretion sensor would need to be immune to the presence of water.

Planar Antenna Results

To further demonstrate the robustness of the sensing method, experiments were also performed using the microstrip patch antenna designs on FR-4 and Rogers RO3003 as described in Chapter Three. From a mechanical standpoint, a planar antenna was more desirable than a waveguide-to-coax adapter because of the smaller size. The antennas would need to be ruggedized in order to survive inside the engine. Results obtained in the following experiments were meant to show the feasibility of using planar antennas with the microwave radiometer. Microstrip patch antennas were fabricated on both substrates so that their performance could be directly compared. The first experiment used the FR-4 microstrip patch antenna on the stator vane assembly. The temperature profile of the ETC, amounts of water, and center frequency of 10 GHz were the same as the first experiment with the prototype process seal insert. The reference load was located inside the ETC to reduce the effect of the temperature fluctuation inside the radiometer enclosure. The data collected was comparing the radiometer antenna to a reference at the same physical temperature. Fig. 37 shows the experimental results as a plot of voltage versus time.

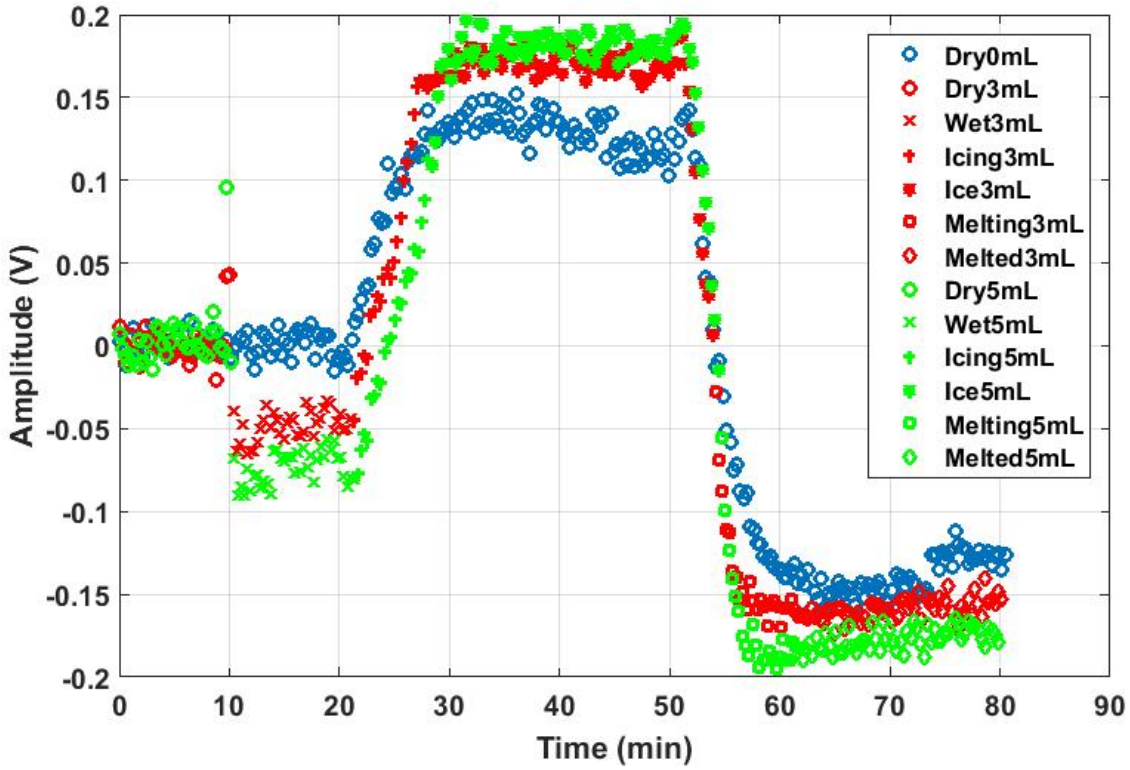

Fig. 37. Voltage vs time plot for water to ice to water experiment using FR-4 microstrip patch antenna.

The trend of the dry run results (blue line) was consistent with previous results. Water and ice yielded the opposite response than what was expected. Fig. 37 suggested that water made the antenna brighter, and ice made the antenna less bright. Both components were still detectable, just not in the same way as with a waveguide-to-coax adapter. The amplitude range was only 0.4 V, which was smaller than previous experiments. FR-4 has considerable losses, so it made sense that the amount of energy received by the antenna would be less than an unfilled waveguide-to-coax adapter. An experiment was conducted using the microstrip patch antenna on a Rogers RO3003 substrate. Results from this experiment are shown in Fig. 38. It should be noted that the ETC only spent 20 minutes at 10°C as opposed to the normal 30 minutes.

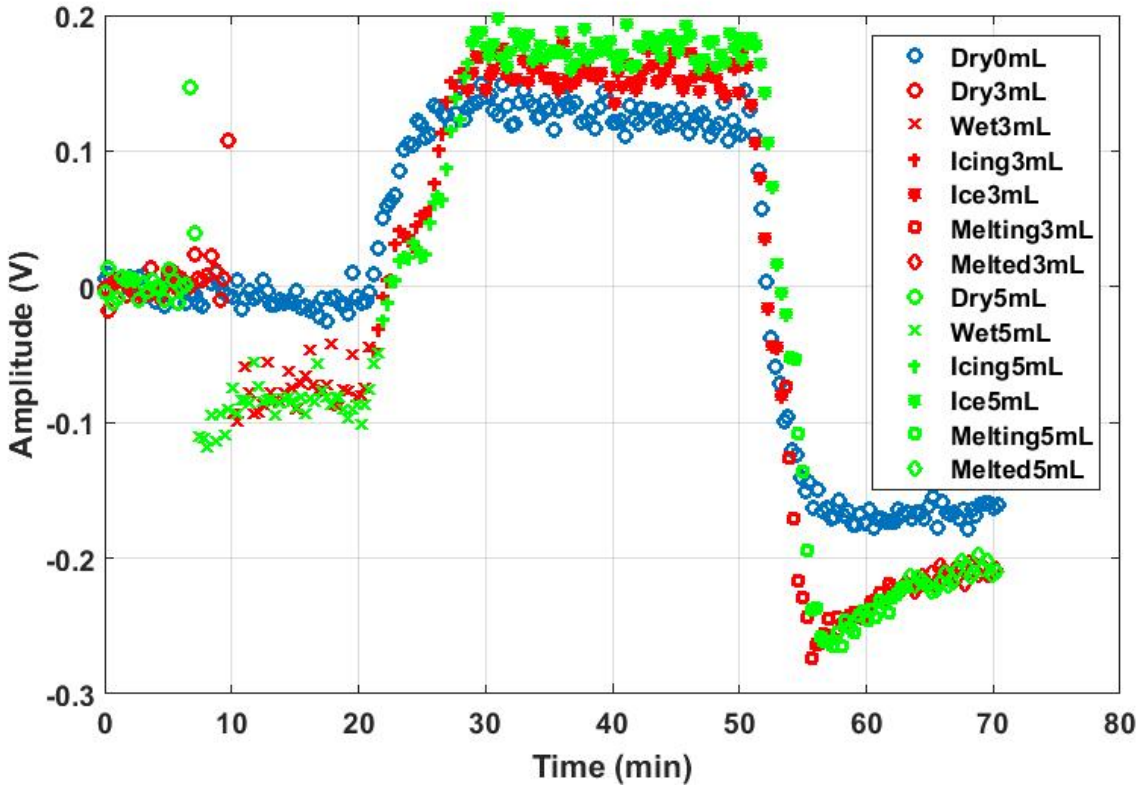

Fig. 38. Voltage vs time plot for water to ice to water experiment using Rogers RO3003 microstrip patch antenna.

The 0.6 V amplitude range for the RO3003 microstrip patch antenna was greater than the FR-4 microstrip patch antenna. Lower dielectric loss in the Rogers RO3003 substrate allowed the radiometer to receive more energy. The lack of separation for the different volumes of water was caused by the 5 mL of water spreading out beyond the antenna beam width while melting. Water could still be detected as separate from the dry response, but a similar phenomenon was observed where the effects of water and ice on the antenna brightness temperature were flipped. Mounting the planar antenna, which typically would radiate in free space, to the stator vane assembly resulted in unexpected changes in the sensor's response. The physical properties of water and ice are constant,

therefore the planar antenna had to be causing the change. Further study of planar antennas is suggested in Chapter Five.

CHAPTER FIVE

Conclusion

A wide-band microwave radiometer has been developed to sense ice accretion inside a turbofan jet engine. The sensor's ability to detect water and ice has been demonstrated while considering the harsh measurement environment. Experimental data pointed to 10 GHz as the best center frequency for consistent detection. Multiple radiometer antenna designs have been tested in an engine-like geometry. Future experiments should include demonstrating immunity to Doppler effects, changing the polarization of the antenna, testing the minimal amount of ice needed for detection, and changing the location of the ice on the stator vane assembly (e.g. on the sides of the vanes).

The ice accretion sensor presented here has the potential to enhance the safety of air travel. Knowing when ice has begun to accrete inside a turbofan jet engine before rollback occurs is paramount to avoid engine powerloss events at altitude. In addition to being used in real flight scenarios, the ice accretion sensor could also be used in icing tests of new engine designs. Data from the sensor could validate an engine's resilience to ice accretion at different stages of its compressor. Practically, there would need to be multiple antennas in the engine because ice accretion is not guaranteed to be uniform. The microwave radiometer system could easily be adapted to handle inputs from multiple antennas, so another sensor would not be needed.

Exceptionally promising results were obtained using the prototype process seal insert as the radiometer antenna. The microwave radiometer detected ice unambiguously with a similar difference between dry and iced vanes that was seen with the un-filled waveguide-to-coax adapter. On average, the presence of ice created an 80 mV difference from dry vanes with the prototype process seal insert. A new antenna should be fabricated from this design with ruggedization and size in mind. The coaxial probe and process seal insert can be fabricated as one piece to reduce the size. In addition, the process seal insert geometry could be adapted to withstand pressure from the front face, such as a small expansion of the aperture at the engine interface.

One shortcoming of this work was the unexplained results from the planar antennas. Water and ice produced the opposite sensor response than what was expected. The geometry of the stator vane assembly seems to have a significant impact on the planar antennas. There are several possible causes for the discrepancies in the planar antenna results: incorrect polarization, impedance matching issues, or sensitivity to other things in the test chamber. It is difficult to predict these effects in simulation because the antennas are being used with a passive sensor. Further testing of the planar antennas is therefore needed, and should include: changing the antenna polarization on the stator vane assembly, electrically isolating the stator vane assembly, and experimenting with a circularly polarized antenna. The results from these experiments should shed some light on the unidentified issues experienced.

Design Improvements

There are multiple ways in which the ice accretion sensor can be improved upon from its current state. First, there are several components that need to be added to the

microwave radiometer design. An RF bandpass filter with a center frequency of 10 GHz and approximately 1.2 GHz 3 dB bandwidth can be added to the RF chain before the RF amplifier. The filter will have some insertion loss, but it will isolate the frequency band of interest around 10 GHz. Given the choice of center frequency based on experimental results, a 10 GHz oscillator with output power of at least +10 dBm should be implemented as the LO input to the mixer. The VNA provided flexibility in testing multiple center frequencies, but that functionality is no longer needed. Condensing the LO into a single oscillator would greatly reduce the system's size. The power supply to the microwave radiometer could also be redesigned. Inadequate voltage regulation and heat dissipation led to issues during testing at times. An external 24 V AC/DC adapter could be considered in order to reduce the necessary size of the radiometer enclosure. New linear voltage regulators and heat sinks would alleviate the issue of overheating.

Second, a microwave radiometer design using surface mount components on a printed circuit board should be completed. The current dimensions of the enclosure make it impractical to implement on an airplane. Each connectorized component could be replaced with a similar surface mount component. For example, the Mini-Circuits ZX05-24MH+ wideband mixer could be replaced by an Analog Devices HMC1056LP4BE surface mount mixer. The printed circuit board design could be broken into the different chains of the microwave radiometer. There could be a separate board for the RF chain, IF chain, power, etc. to make the entire design modular. Total physical size of the enclosure could be reduced to less than 1 ft^3.

Third, the front end components (up to and including the RF amplifier) could be integrated with the microwave radiometer antenna. For example, if a planar antenna were

used as the radiometer antenna, the front end components could be soldered to the back-side. If a waveguide-to-coax adapter with a process seal insert were used, then a flexible PCB with the surface mount front end could be wrapped around it. Doing so would eliminate the SMA cables from the antenna inside the test chamber to the radiometer enclosure which increases the radiometer's sensitivity.

APPENDICES

APPENDIX A

Mechanical Drawings

Mechanical drawings of the stator vane assembly and waveguide taper section are shown in the following pages. The drawings were produced in SolidWorks, a 3D CAD modeling software. All dimensions are in inches.

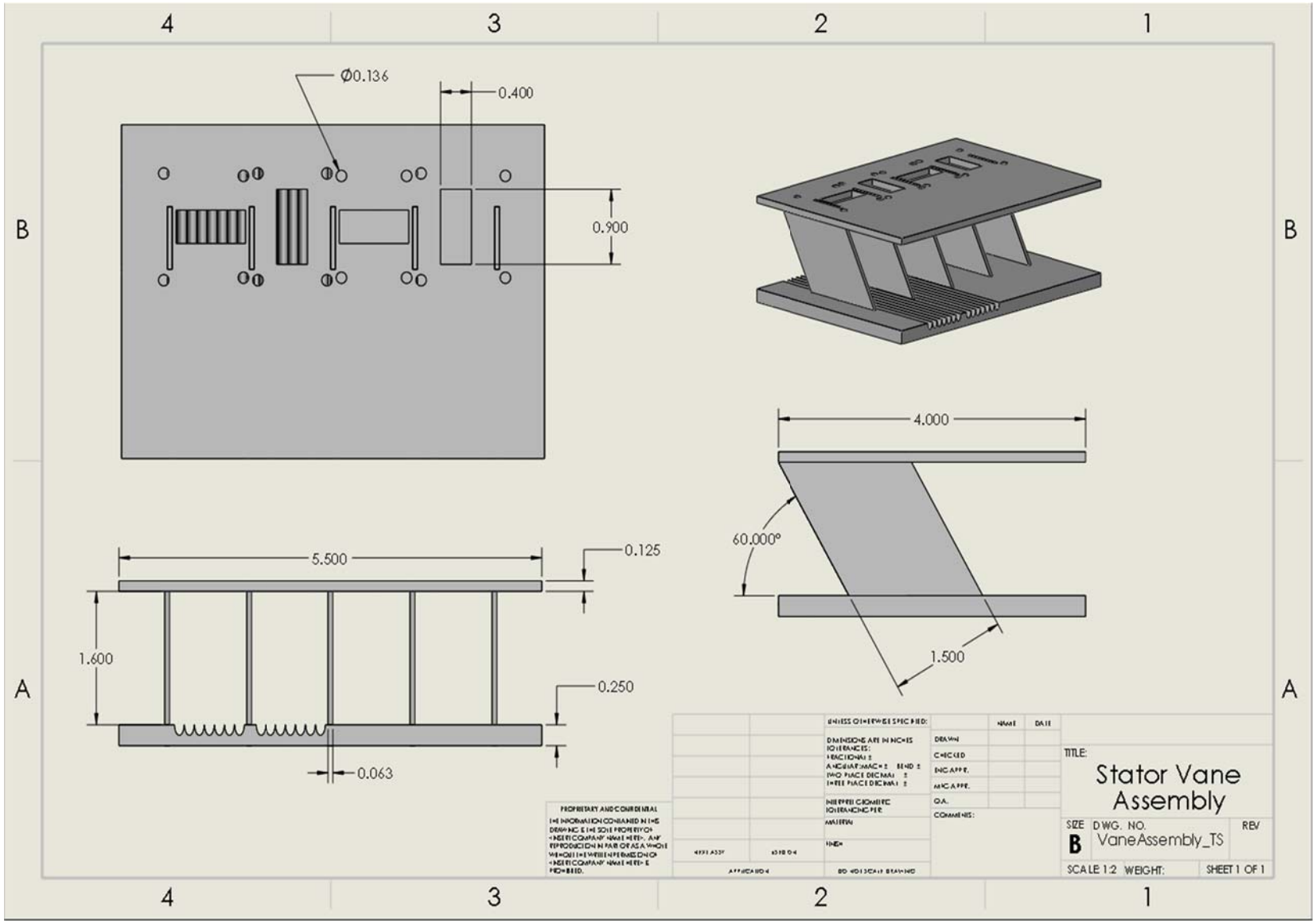
4
3
2
1
B
A
Ø0.136
0.400
0.900
4.000
60.000°
1.500
5.500
0.125
1.600
0.250
0.063
UNLESS OTHERWISE SPECIFIED:
DIMENSIONS ARE IN INCHES
TOLERANCES:
FRACTIONAL ±
ANGULAR: MACH ± BEND ±
TWO PLACE DECIMAL ±
THREE PLACE DECIMAL ±
INTERPRET GEOMETRIC TOLERANCING PER:
MATERIAL
FINISH
NEXT ASSY
USED ON
APPLICATION
DO NOT SCALE DRAWING
NAME
DATE
DRAWN
CHECKED
ENG APPR.
MFG APPR.
Q.A.
COMMENTS:
PROPRIETARY AND CONFIDENTIAL
THE INFORMATION CONTAINED IN THIS DRAWING IS THE SOLE PROPERTY OF <INSERT COMPANY NAME HERE>. ANY REPRODUCTION IN PART OR AS A WHOLE WITHOUT THE WRITTEN PERMISSION OF <INSERT COMPANY NAME HERE> IS PROHIBITED.
TITLE:
Stator Vane Assembly
SIZE
B
DWG. NO.
VaneAssembly_TS
REV
SCALE: 1:2
WEIGHT:
SHEET 1 OF 1

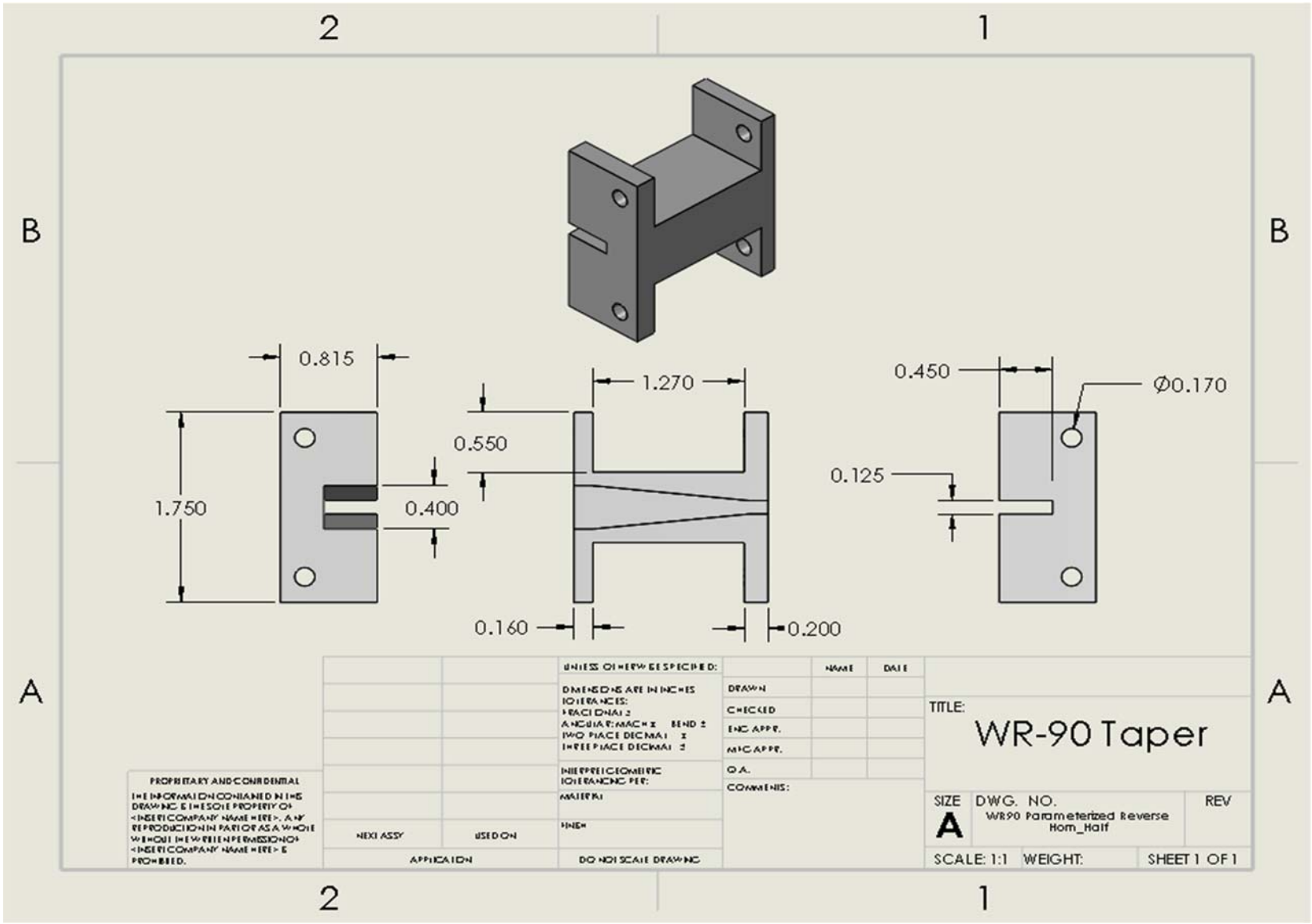
2
1
B
A
0.815
1.750
0.400
1.270
0.550
0.160
0.200
0.450
Ø0.170
0.125
UNLESS OTHERWISE SPECIFIED:
DIMENSIONS ARE IN INCHES
TOLERANCES:
FRACTIONAL ±
ANGULAR: MACH ± BEND ±
TWO PLACE DECIMAL ±
THREE PLACE DECIMAL ±
INTERPRET GEOMETRIC TOLERANCING PER:
MATERIAL
FINISH
NEXT ASSY
USED ON
APPLICATION
DO NOT SCALE DRAWING
NAME
DATE
DRAWN
CHECKED
ENG APPR.
MFG APPR.
Q.A.
COMMENTS:
TITLE:
WR-90 Taper
SIZE
A
DWG. NO.
WR90 Parameterized Reverse Horn_Half
REV
SCALE: 1:1
WEIGHT:
SHEET 1 OF 1
PROPRIETARY AND CONFIDENTIAL
THE INFORMATION CONTAINED IN THIS DRAWING IS THE SOLE PROPERTY OF <INSERT COMPANY NAME HERE>. ANY REPRODUCTION IN PART OR AS A WHOLE WITHOUT THE WRITTEN PERMISSION OF <INSERT COMPANY NAME HERE> IS PROHIBITED.

APPENDIX B

Bill of Materials

This section contains the major components of the microwave radiometer. Small components such as individual capacitors or resistors have been omitted. Some components are no longer available from the manufacturer, therefore the cost was not included.

Table 4. Microwave radiometer bill of materials

Component	Manufacturer	Manufacturer P/N	Vendor	Cost
RF (Dicke) Switch	Analog Devices	HMC-C011	Digi-Key	$1,967.83
50 Ω Reference Load	Midwest Microwave	TRM-2003-F0-SMA-07	-	-
RF Amplifier	Mini-Circuits	ZVA-213+	Mini-Circuits	$995.00
Mixer	Mini-Circuits	ZX05-24MH-S+	Mini-Circuits	$54.95
Local Oscillator	HP	HP-8720ET	-	-
IF Amplifier	Amplical	AMP001G2-30	Amplical	$2,000.00
Low-Pass Filter	Lorch Microwave	4LP7-600-S	Lorch Microwave	-
IF Amplifier	Mini-Circuits	ZX60-3018G-S+	Mini-Circuits	$49.95
Detector Diode	Pasternack	PE8010	Pasternack	$444.30

BIBLIOGRAPHY

[1] J. G. Mason, J. W. Strapp and P. Chow, "The Ice Particle Threat to Engines in Flight," in *44th AIAA Aerospace Sciences Meeting and Exhibit*, Reno, 2006.

[2] R. V. Goodwin and D. Fuleki, "Engine Preparation and Instrumentation for the Second Ice Crystal Engine Test at NASA PSL-3 Test Facility," in *8th AIAA Atmosphere and Space Environments Conference*, Washington, D.C., 2016.

[3] UTC Aerospace Systems, "Ice Detector Model 0871LH1," 2013. [Online]. Available: utcaerospacesystems.com/cap/systems/sisdocument/Ice%20Detection%20and%20Protection%20Systems/Ice%20Detector%20Model%20200871LH.pdf. [Accessed 21 February 2017].

[4] N. Skou and D. L. Vine, Microwave Radiometer Systems, Norwood, MA: Artech House, Inc., 2006.

[5] F. T. Ulaby, R. K. Moore and A. K. Fung, Microwave Remote Sensing: Fundamentals and Radiometry, vol. I, Reading, Massachusetts: Addison-Wesley Pub. Co., 1981, p. 456.

[6] R. H. Dicke, "The Measurement of Thermal Radiation at Microwave Frequencies," *The Review of Scientific Instruments,* vol. 17, no. 7, pp. 268-279, 1946.

[7] C. A. Balanis, Advanced Engineering Electromagnetics, Hoboken, NJ: John Wiley & Sons, Inc., 2012, p. 41.

[8] D. M. Pozar, Microwave Engineering, 3rd ed., Hoboken, NJ: John Wiley & Sons, Inc., 2005, p. 1.

[9] S. Pinon, D. L. Diedhiou, A. M. Gue, N. Fabre, G. Prigent, V. Conedera, E. Rius, C. Quendo, B. Potelon, J. F. Favennec and A. Boukabache, "Development of a Microsystem based on a Microfluidic Network to Tune and Reconfigure RF Circuits," *Journal of Micromechanics and Microengineering,* vol. 22, no. 7, 2012.

[10] U. Kaatze, "Complex Permittivity of Water as a Function of Frequency and Temperature," *Journal of Chemical and Engineering Data,* vol. 34, no. 4, pp. 371-374, 1989.

[11] P. Debye, Polar Molecules, New York: Dover, 1929.

[12] W. J. Ellison, "Permittivity of Pure Water, at Standard Atmospheric Pressure, over the Frequency Range 0-25 THz and the Temperature Range 0-100°C," *Journal of Physical and Chemical Reference Data,* vol. 36, no. 1, 2007.

[13] A. D. Watt and E. L. Maxwell, "Measured Electrical Properties of Snow and Glacial Ice," *Journal of Research of the National Bureau of Standards,* vol. 64D, no. 4, pp. 357-363, 1960.

[14] S. Fujita, T. Matsuoka, S. Morishima and S. Mae, "The Measurement on the Dielectric Properties of Ice at HF, VHF and Microwave Frequencies," in *Geoscience and Remote Sensing Symposium*, Tokyo, 1993.

[15] W. D. Philpot and W. R. Philipson, "Passive Microwave Sensing," in *Remote Sensing Fundamentals*, 2012.

[16] A. v. Hippel, "The Dielectric Relaxation Spectra of Water, Ice, and Aqueous Solutions, and their Interpretation," *IEEE Transactions on Electrical Insulation,* vol. 23, no. 5, pp. 825-840, 1988.

[17] L. R. Ballew, *A Microwave Radiometer System for Use in Biomedical Applications,* Waco: Baylor University, 2006.

[18] S. Steinke, U. Lohnert, S. Crewell and S. Liu, "Water Vapor Tomography with Two Microwave Radiometers," *IEEE Geoscience and Remote Sensing Letters,* vol. 11, no. 2, pp. 419-423, 2014.

[19] L. Zhang, T. Zhao, L. Jiang and S. Zhao, "Estimate of Phase Transition Water Content in Freeze-Thaw Process Using Microwave Radiometer," *IEEE Transactions on Geoscience and Remote Sensing,* vol. 48, no. 12, pp. 4248-4255, 2010.

[20] A. Kontu and J. Pulliainen, "Simulation of Spaceborne Microwave Radiometer Measurements of Snow Cover Using In Situ Data and Brightness Temperature Modeling," *IEEE Transactions on Geoscience and Remote Sensing,* vol. 48, no. 3, pp. 1031-1044, 2010.

[21] R. V. Goodwin and D. Fuleki, "Engine Preparation and Instrumentation for the Second Ice Crystal Engine Test at NASA PSL-3 Test Facility," in *8th AIAA Atmospheric and Space Environments Conference*, Washington, 2016.

[22] *CST Microwave Studio 2016,* Computer Simulation Technology.

[23] S. M. Wentworth, Applied Electromagnetics Early Transmission Lines Approach, Hoboken, NJ: John Wiley & Sons, Inc., 2007.

[24] R. E. Munson, "Microstrip Antennas," in *Antenna Engineering Handbook*, McGraw-Hill, Inc., 1993, pp. 7-2.

[25] D. R. Jackson, "Microstrip Antennas," in *Antenna Engineering Handbook*, McGraw-Hill, 2007, p. 175.